Influence of flaw inclination angle and loading condition on crack initiation and propagation

Huanqiang Li, Louis Ngai Yuen Wong *

School of Civil and Environmental Engineering, Nanyang Technological University, Singapore 639798, Singapore

ABSTRACT

With reference to the experimental observation of crack initiation and propagation from pre-existing flaws in rock specimens under compression, the influences of pre-existing flaw inclination angle on the cracking processes were analyzed by means of finite element method (FEM) and non-linear dynamics method. FEM analysis on the stress field distribution induced by the presence of a pre-existing flaw provided better understanding for the influence of flaw inclination angle on the initiation position and initiation angle of the potential cracks. Numerical analysis based on the non-linear dynamics method was performed to simulate the cracking processes. The resultant crack types, crack initiation sequences and the overall crack pattern were different under different loading conditions. Under a relatively low loading rate or a small magnitude of maximum loading pressure, tensile cracks would tend to initiate prior to shear cracks. In contrast, under a relatively high loading rate and a large magnitude of maximum loading pressure, shear cracks would tend to initiate prior to tensile cracks instead.

© 2012 Elsevier Ltd. All rights reserved.

1. Introduction

Numerous experimental (Bieniawski, 1967; Brace and Bombolakis, 1963; Chen et al., 1993; Huang et al., 1990; Lajtai, 1974; Li et al., 2005; Petit and Barquins, 1988; Rispoli, 1981; Tang, 1997; Wawersik and Fairhurst, 1970; Willemse et al., 1997; Wong and Einstein, 2009b,c; Wong et al., 2006; Zhao et al., 2010) and theoretical efforts (Einstein and Dershowitz, 1990; Hancock, 1985; Ingraffea and Heuze, 1980; Karihaloo, 1979; Kendall, 1978; Radjy and Hansen, 1973; Schreyer, 2007) have been devoted to the study of crack initiation, propagation, interaction and eventual coalescence in rocks in the past decades. The cracking phenomena and crack patterns observed experimentally have served as valuable references for the numerical work. Theoretical studies related to cracking processes can be broadly classified into three categories, namely, development and verification of crack initiation criteria, studies based on analytical methods, and studies based on numerical methods. Most of the studies of crack initiation criteria focus on criteria based on Linear Elastic Fracture Mechanics (LEFM) (Griffith, 1920; Hoelzer et al., 1986; Irwin et al., 1968; Lajtai et al., 1990; Maiti and Smith, 1984; McMillan and Pelloux, 1970; Palmer et al., 1974; Rossmanith, 1983; Sommer and Soltész, 1971; Sullivan and Crooker, 1977; Wang and Shrive, 1995; Wells, 1969) and criteria based on the Materials Strength (MS) (Atkinson, 1987). Compared with the MS criteria, the LEFM criteria have the advantage and

capability of predicting the length of crack propagation (Atkinson, 1987). Its applicability in describing and predicting the propagation and coalescence of multiple cracks in geomaterials is however limited (Tang and Kou, 1998; Wang and Shrive, 1993). On the contrary, MS criteria can be used in materials with certain plastic properties, such as rocks subjected to a high hydrostatic pressure (Nemat-Nasser, 1985). MS criteria can take into account of the hydrostatic pressure-dependent strength property, which is a distinct property of geomaterials. With regard to the numerical calculation, the MS criteria are more convenient to implement than the LEFM criteria. The MS criteria can be used to simulate the cracking phenomenon by considering the microscopic material failure.

Nowadays a number of numerical techniques are available to model cracking processes, such as NMM (Zhang et al., 2010), X-FEM (Rannou et al., 2010), DDA (Pearce et al., 2000), BEM (Chen et al., 1998; Lauterbach and Gross, 1998) PFC (Potyondy and Cundall, 2004), RFPA (Tang, 1997; Tang and Kou, 1998; Tang et al., 2000) and several other in-house codes based on the LEFM criteria (Maligno et al., 2010; Ouinas et al., 2009; Sreeramulu et al., 2010; Weber et al., 2010). As observed in the literature, these codes have been widely applied to the investigation of crack initiation in elastic materials. As shown in our preliminary study (Li and Wong, 2011; Wong and Li, 2011) in assessing the applicability of non-linear dynamics method in simulating cracking processes, the engagement of the MS crack initiation criteria can satisfactorily handle a large strain and plastic deformation behavior in geomaterials. The simulation results matched closely the experimentally observed cracking phenomena. More importantly,

* Corresponding author. Tel.: +65 67905290; fax: +65 67910676.
E-mail address: lnywong@ntu.edu.sg (L.N.Y. Wong).

the initiation of tensile cracks and shear cracks can be differentiated based on the numerical results. Different representative crack types including tensile wing cracks, anti-wing cracks and horsetail cracks can be modeled.

In the present study, the influence of flaw inclination angle in a rock specimen subjected to a uniaxial compression was studied by means of numerical simulations, which aimed at providing the mechanics basis to account for the experimental observations. As observed in most of the previous experimental studies on the influences of pre-existing flaw inclination angle on crack type, crack initiation point and the crack trajectory (Park and Bobet, 2010; Wong, 2008), the investigations were typically conducted under a quasi-static loading condition. In the present study, beside the pre-existing flaw inclination angle, the influence of the loading conditions (loading rate, loading magnitude) applied to the model was also numerically studied. Most of the experimental studies of time-dependent fracturing behavior in the literature focused on the influence of loading rate on fracture toughness or energy (Backers et al., 2003; Bazant and Gettu, 1992; Biolzi and Tognon, 1987; Xia et al., 2008; Yamamoto et al., 2004; Yoon et al., 1999; Zhang et al., 2009; Zhou et al., 2010; Zielinski, 1984). A number of theories have been developed to account for the relevant influence of loading rate (Reinhardt and Weerheijm, 1991; Vanel et al., 2009; Webb and Aifantis, 1970). The subject has also been studied by numerical methods (Chiarelli et al., 1996; Koppenhoefer and Robert, 1997; Ožbolt et al., 2006), which revealed the influences of loading rate on the magnitude of crack initiation load and some crack initiation variables, such as the fracture toughness. However, an in-depth study of shear cracks was typically not involved. On the basis of our previous studies (Li and Wong, 2011; Wong and Li, 2011), we extended the work to analyze the influences of loading rate and loading magnitude on the development and evolution of tensile cracks and shear cracks.

This paper is structured in the following way. In Section 2, through the analysis of stress field around the flaw prior to crack initiation, the influences of pre-existing flaw inclination angle on probable crack initiation position are described. In Section 3, after introducing the fundamentals of the numerical and material models, as well as some of the previous results, the numerical results on the influences of pre-existing flaw inclination angle on crack initiation and propagation are presented. In Section 4, the numerical results on the influences of loading conditions on the crack development are described. Summary (Section 5) and conclusions (Section 6) are provided towards the end of the paper.

2. Inclination angle influence on stress field prior to crack initiation

2.1. FEM models

In order to systematically investigate the cracking processes associated with a 12.7 mm long open pre-existing flaw located in the middle of the model, the stress field in the vicinity of the pre-existing flaw and along its perimeter was first numerically determined by the elastic finite element method (FEM). The 2D plain strain FEM model was built in ANSYS based on the models of previous experimental studies (Wong and Einstein, 2009a,b) (Fig. 1). The dimensions of the numerical model were 150 mm × 75 mm. A vertical pressure (σ_0) was applied at the top and bottom boundaries of the numerical model. A total of nineteen cases of the numerical model were analyzed, all of which contained a differently-inclined flaw, ranging from flaw inclination angle $\theta = 0–90°$, at 5° increment. The parameters in elastic material model are as follows: density = 2.44 g/cm^3, bulk modulus = 2.7E + 07 kPa, shear modulus = 2.2E + 07 kPa.
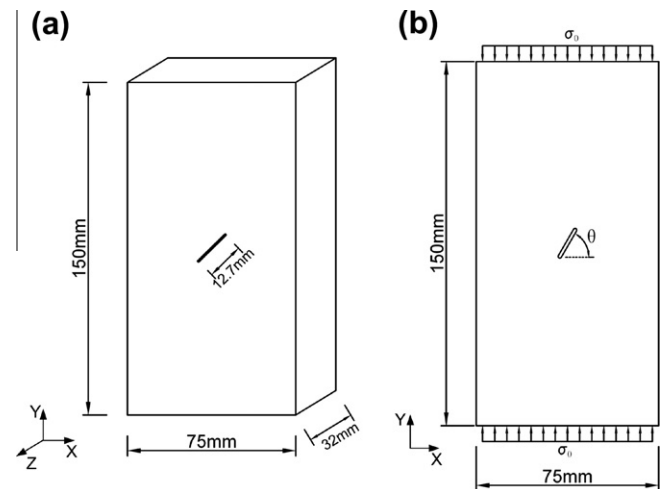

Fig. 1. Dimensions of (a) physical testing model and (b) numerical model. The flaw width was 1.3 mm.

2.2. Stress field around a pre-existing flaw

Generally speaking, when the tensile stress reaches the material tensile strength, the material will fail and a tensile crack initiates. The third principal stress (tensile stress) thus has a strong influence on the initiation of tensile cracks in rock. Based on our previous study (Li and Wong, 2011; Wong and Li, 2011), the initiation and propagation of cracks can be predicted by the consideration of pressure, Mises stress (equivalent stress) and yield stress. In order to better understand the crack initiation process, the third principal stress, pressure and Mises stresses around the perimeter of differently-inclined flaws were obtained from the FEM analysis and were examined in detail. In this paper, unless noted otherwise, pressure (P) is defined as the average of three principal stresses ($\sigma_1, \sigma_2, \sigma_3$), i.e. $P = (\sigma_1 + \sigma_2 + \sigma_3)/3$. The principal stress vector plot (Fig. 2) based on the FEM analysis reveals that the direction of the third principal stress (tensile stress) on the flaw perimeter is generally parallel to the flaw perimeter in the tensile area.

Besides directions, the magnitude of tensile stress on the flaw perimeter was also determined numerically. To show the degree of tensile stress concentration, the ratio of the third principal stress (σ_3) along the flaw perimeter to the externally applied loading stress (σ_0) was studied. The position along the flaw perimeter was represented by a value ranging from 0 to 1 between the two flaw tips (Fig. 3). Only the top half of the flaw perimeter was analyzed due to symmetry.
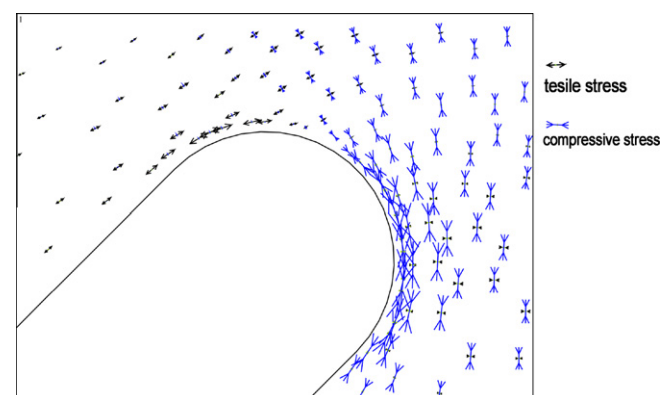

Fig. 2. A principal stress vector plot around a pre-existing flaw tip.
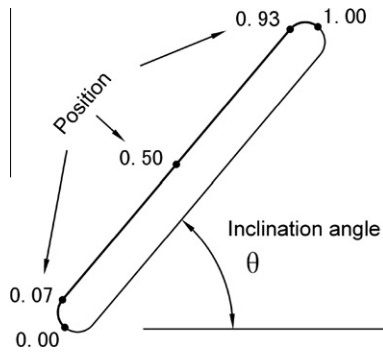
Fig. 3. Definition of the position along the flaw perimeter and the flaw inclination angle in the FEM analysis.

The dependency of the stress ratio σ_3/σ_0 along the flaw perimeter on the position and flaw inclination is illustrated by plotting the FEM numerical results in a 3-dimensional (3D) space versus the position along the perimeter (0–1) and the flaw inclination angle (0–90°) (Fig. 4). Notice that compressive stress is positive and tensile stress is negative in the present study. The plot in Fig. 4 reveals that the highest tensile stress (most negative σ_3/σ_0) occurs at positions between 0.8 and 1.0 along the perimeter of the flaw, which has an inclination angle between 30° and 50°. Alternatively, the 3D plot can be transformed to a 2D plot by showing the stress ratios in a contoured profile (Fig. 5). For each flaw inclination angle, the maximum ratios of third principal stress (σ_3), tensile pressure (σ_t), compressive pressure (P) and Mises stress (σ_v) to the externally applied loading stress (σ_0), and the corresponding position on the flaw perimeter were determined and summarized in appendix.

If the maximum tangential stress criterion similar to that developed by Erdogan and Sih (1963) is used to model the crack initiation phenomenon, the position corresponding to the maximum third principal stress (tensile stress) along the flaw perimeter will be the tensile crack initiation position. Based on the results in appendix, tensile crack initiation is the most favorable for a flaw inclined at $\theta = 40°$. The corresponding crack initiation position will be at around 0.94 on the flaw perimeter. Refer also to the side sketches of the stress ratio plots along $\theta = 40°$ and flaw position = 0.94 in Fig. 5.
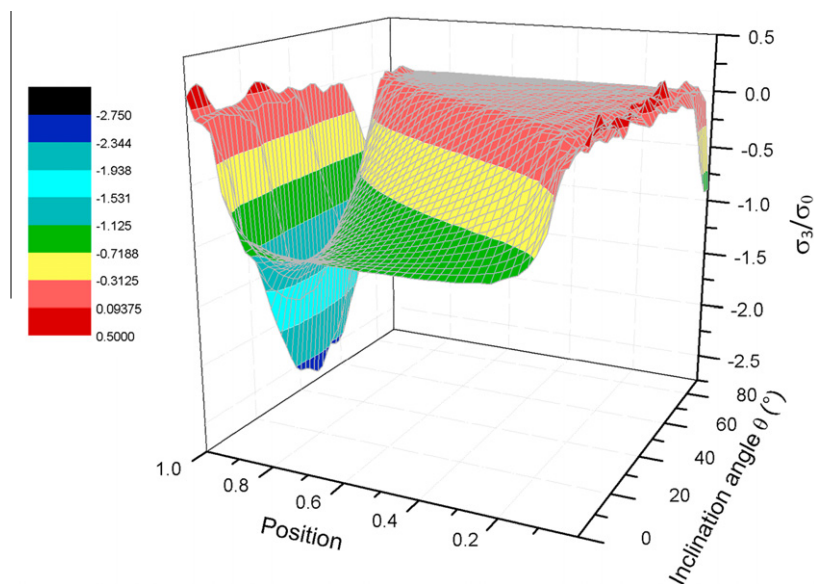
Recall that the pressure (P) is defined as the average of three principal stresses ($\sigma_1, \sigma_2, \sigma_3$), i.e. $P = (\sigma_1 + \sigma_2 + \sigma_3)/3$. The pressure P is similarly represented on a contoured plot versus position along the flaw perimeter and flaw inclination (Fig. 6). Refer also to columns 4–7 under the heading of "maximum pressure (P)" in appendix for the numeric values. According to the data listed in appendix, the position where the maximum normalized tensile pressure (P/σ_0) on the flaw perimeter occurs is the same position where the maximum normalized σ_3/σ_0 occurs. That indicates that both the tensile pressure and the σ_3 can be used to describe the variation of tensile stress.

A contoured plot of Mises stress (σ_v) versus position along the flaw perimeter and flaw inclination is obtained and shown in Fig. 7. The maximum Mises stress occurs for a flaw inclined at around 0°, i.e. horizontal flaw; and the corresponding position is around the flaw tips. Refer also to columns 8 and 9 under the heading of "maximum Mises stress (σ_v)" in appendix for the numeric values.

2.3. Probable crack initiation position

In our previous study (Li and Wong, 2011; Wong and Li, 2011) on crack initiation mechanisms with reference to experimental studies, the tensile crack initiation was satisfactorily modeled to be induced by the local increase of tensile stress. Shear crack initiation was satisfactorily modeled to be induced by the local increase of Mises stress, whose rate of increase is higher than that of the yield stress. The present FEM numerical study of the maximum tensile stress and Mises stress distribution, in combination with the previous study, thus enabled the prediction of the initiation position of tensile crack and shear crack from a pre-existing flaw in compression.

With reference to the numeric values presented earlier in appendix, Fig. 8 illustrates the crack initiation position for different flaw inclinations, assuming that the initiation position of tensile crack and shear crack correspond to where the maximum tensile stress and maximum Mises stress occur respectively. Fig. 8(a) reveals that for the flaws of small inclination angles (θ), tensile cracks tend to initiate from the flaw center, at a considerable distance away from the flaw tip. As the flaw becomes steeper, i.e. θ ranging from 20° to 90°, the tensile crack initiation position will
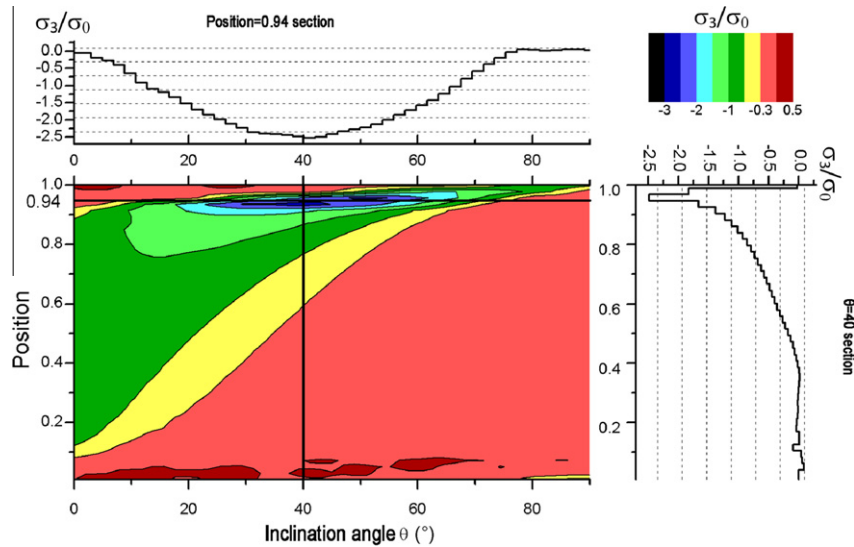

Fig. 4. 3D contour plot of stress ratio σ_3/σ_0 versus position along the flaw perimeter and flaw inclination.

Fig. 5. 2D contour plot of stress ratio σ_3/σ_0 versus position along the flaw perimeter and flaw inclination.
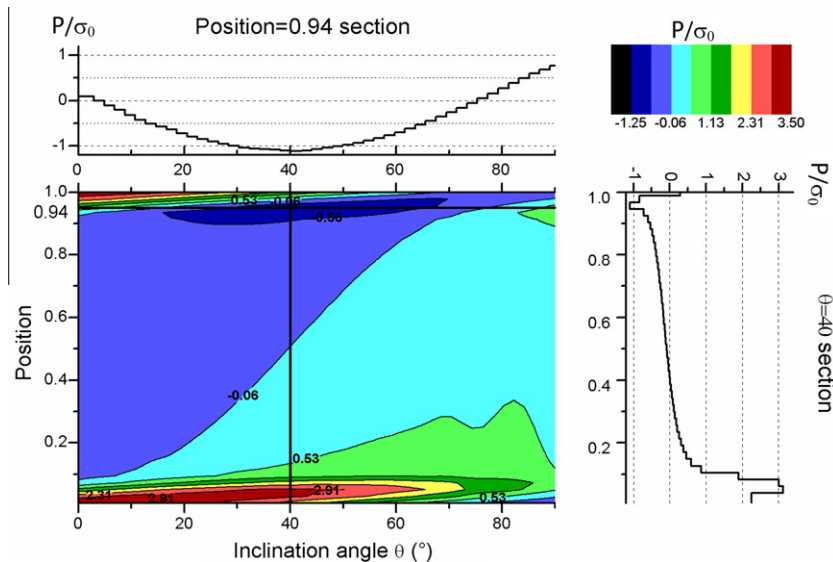

Fig. 6. 2D contour plot of pressure ratio (P/σ_0) versus position along the flaw perimeter and flaw inclination.

be close to or at the circular flaw tip region. In contrast, as shown in Fig. 8 (b), the shear crack initiation position for the entire range of θ ranging from 0° to 90° is restricted to the circular flaw tip region. For $\theta = 0°$, i.e. horizontal flaw, the shear crack initiation position is right at the flaw tip. As θ increases, the crack initiation position gradually shifts away from the flaw tip towards the straight edge of the flaw.

The above results can be alternatively illustrated in the sketches in Fig. 9, each of which corresponds to a particular flaw inclination angle. On each of these pre-existing flaws, the locations corresponding to the maximum tensile stress and maximum Mises stress are marked as a solid circle and an open circle, respectively. Based on these sketches, the crack initiation position for the tensile cracks and shear cracks can be generalized with the illustrative sketch of Fig. 9(g). In that sketch, which shows a 2D plane strain model of a straight open flaw with a rounded tip, the shear crack initiation position is always at the point where the maximum principal stress direction is tangent to the flaw perimeter. The tensile crack initiation position, on the other hand, is more complicated

to generalize. If the flaw is symmetrical with respect to the maximum principal stress direction, such as the cases of a horizontal flaw ($\theta = 0°$) and a vertical flaw ($\theta = 90°$), the tensile crack initiation position will be the point where the perpendicular line to the maximum principal stress is tangent to the flaw perimeter. For other flaw inclination angles, i.e. the flaws are asymmetrical to the maximum principal stress directions, the tensile crack initiation position will deviate from the tangent point to the flaw perimeter. The deviated distance (marked as 'd' in Fig. 9(g)) varies with the flaw inclination angle and it becomes smaller for steeper flaws, i.e. larger θ.

3. Simulation of cracking processes

3.1. Numerical models and previous study

3.1.1. Numerical methods

The above elastic FEM analysis provides comprehensive information of the stress fields prior to the crack initiation, without
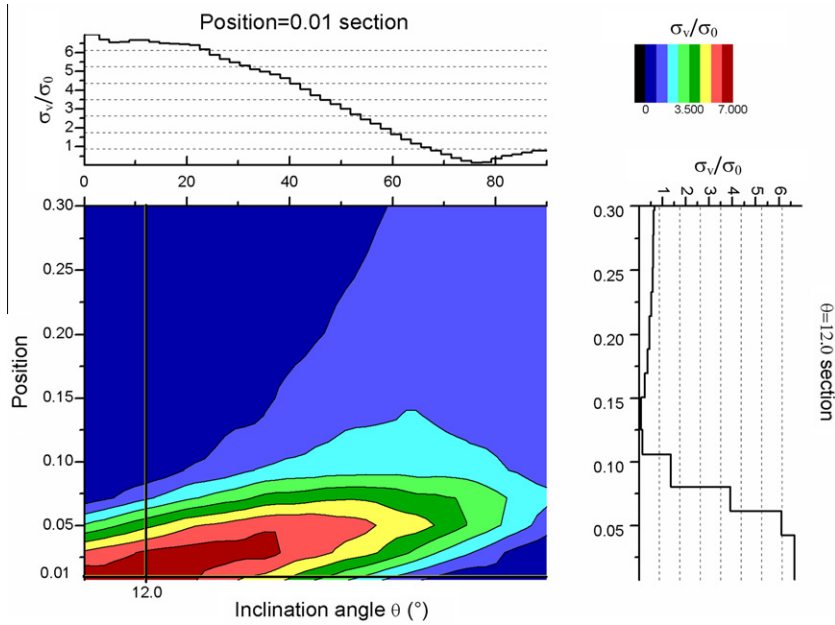
Fig. 7. 2D contour plot of Mises stress $(\sigma_v)/\sigma_0$ versus position along the flaw perimeter and flaw inclination.
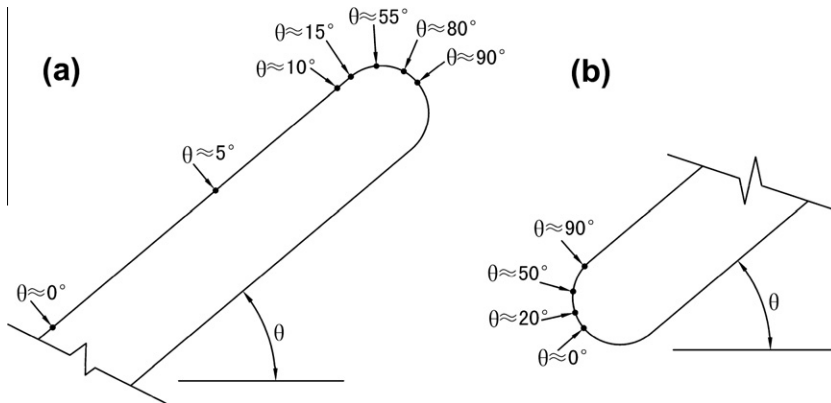

Fig. 8. Crack initiation position for different flaw inclination angles θ corresponding to (a) maximum tensile stress for tensile crack initiation, and (b) maximum Mises stress for shear crack initiation.
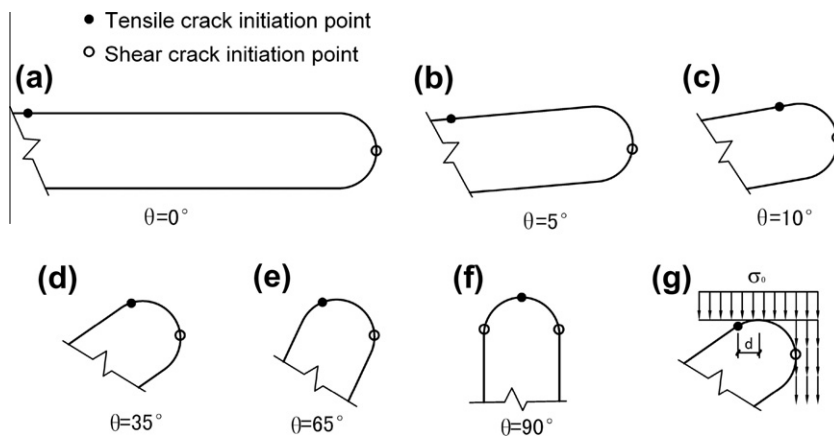

Fig. 9. Initiation position of tensile crack (solid circle) and shear crack (open circle) for differently oriented pre-existing flaws.

the consideration of yielding and failure in material. Once a crack has initiated from the pre-existing flaw, the stress field around the pre-existing flaw will change. In other words, the early cracks initiated will influence the subsequent cracking processes. To take

account of this influence and simulate the progressive crack initiation and propagation, the simulation tool must be equipped with proper material models which can reasonably reflect the properties of rock and cracks. In addition, the tool should be able to handle large strains and deformations in the material in response to loading. The software AUTODYN, which is a non-linear dynamics hydrocode satisfying these requirements, was chosen for this study. In this code, the response of the medium subjected to a dynamic loading is governed by the conservation of mass, momentum and energy, in addition to the equation-of-state and constitutive relation of the medium (Tham, 2005). AUTODYN encompasses a wide range of material modeling capabilities. It excels in solving a wide variety of problems characterized by both geometric non-linearities and material non-linearities.

3.1.2. Material models

A competent material model should be able to describe the confinement-dependent strength property and cracking phenomena in rocklike materials. The Drucker–Prager strength model, which excels in these aspects, is adopted in the present study. In the previous Scanning Electron Microscope (SEM) experimental observation of the microcrack development in Carrara marble under compression (Wong and Einstein, 2009b), the development macroscopic cracks observable by unaided eyes is preceded by the development of microcracks along some white patches. Under further loading, the development, propagation and coalescence of the micro cracks form the macro cracks. The initiation of macro crack is therefore not an abrupt event, but associated with a process of cumulative damage. In the present study, cumulative damage (CD) failure criterion is chosen to describe the material failure (cracking) in rocklike materials. The Drucker–Prager strength model and cumulative damage (CD) failure criterion are both offered in AUTODYN.

The CD failure criterion was introduced by Persson (1991) to describe the macroscopic inelastic behavior of material, in which the strength of the material can be significantly degraded by crushing. To model the progressive cracking and subsequent weakening of materials, the CD failure criterion computes a damage factor D, which is related to the amount of straining the material has undergone. The damage factor D, is zero when the effective plastic strain (EPS) is less than a particular value, i.e. $EPS1$ as shown in Fig. 10. When the strain exceeds $EPS1$, the damage factor D increases linearly with strain up to a maximum value D_{max} (<1), which corresponds to an effective plastic strain $EPS2$ (Fig. 10). The relationship is shown in the following expression

$$D = D_{max}\left(\frac{EPS - EPSI}{EPS2 - EPS1}\right) \tag{1}$$

The current value of the damage factor D is then used to modify the bulk modulus, shear modulus and yield strength of the material. The original yield strength (Y) is reduced to Y_{dam}. If the hydrostatic pressure is positive,

$$Y_{dam} = Y(1 - D) \tag{2}$$

If the hydrostatic pressure is negative,

$$Y_{dam} = Y\left(1 - \frac{D}{D_{max}}\right) \tag{3}$$

The bulk modulus and shear modulus are unaffected in compression, while in tension they are progressively reduced to zero when damage is completed. A fully damaged material possesses some residual strength in compression but none in tension. In tension the damaged material is "void" because its strength and modulus are zero. In compressive stress situation, the damaged material still possesses a residual strength. It is in close accordance with the realistic properties of cracks in rock, i.e., when failure (cracking) occurs
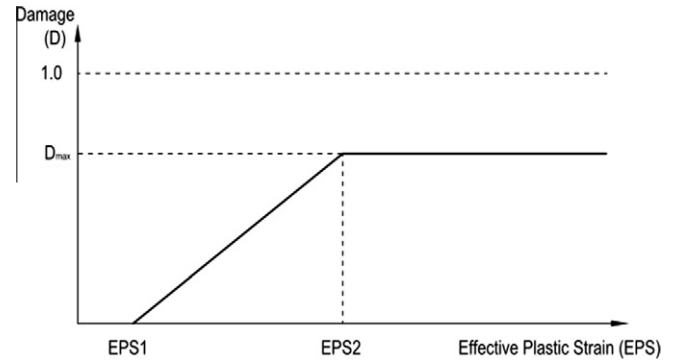

Fig. 10. Cumulative damage as a function of effective plastic strain.

in the model, the model is no longer a continuum model in mechanics, but a model with discontinuities.

Material parameters used in the simulation, including equation of state, material strength and failure criterion, were provided in Table 1. The parameters in the equation of state were obtained by the laboratory test. The material strength parameters, which made reference to those of rock-like material embedded in AUTODYN, were modified according to the laboratory test results. In Table 1, each pair of pressure and yield stress represents a point in pressure and yield stress space which is used to form the material strength line in Drucker–Prager model. The parameters in failure criterion were obtained by trial and error to match the laboratory test results.

3.1.3. Previous study and rationality of the simulation

In our previous study (Li and Wong, 2011; Wong and Li, 2011), crack initiation and propagation are simulated in models consisting of a triangular unstructured-mesh and a material model composed of the Drucker–Prager strength criterion and CD failure criterion (DPCD material model). As shown in Fig. 11, the two crack patterns of the experimental results are comparable to the numerical results, which indicated that the numerical model engaged in the AUTODYN simulation was competent for the study of crack initiation and propagation. Refer to Li and Wong (2011) and Wong and Li (2011) for detailed discussion of the uniqueness of the crack types.

The implementation and results of the loading experiments, against which the numerical results in the present paper are compared, were described in detail by Wong and Einstein (2006, 2009a,b). In the experimental studies, the prepared rectangular pre-cracked Carrara marble specimens were loaded uniaxially in a Baldwin 200 Kips Loading Machine, which was controlled by the computer program MTESTWindows™ (Fig. 12). Load and displacement data were automatically logged at a rate of 2000 samples/min. The properties of Carrara marble are – Poisson's ratio = 0.19; Young's modulus (dynamic) = 49 GPa; and dry density = 2.7 g/cm³. In each loading test, the specimen was continuously loaded and the front face of the specimen was continuously monitored and recorded by a camcorder and a high speed camera.

In our previous numerical study (Li and Wong, 2011; Wong and Li, 2011), tensile cracks and shear cracks can be satisfactorily differentiated by the respective unique relations of the pressure, Mises stress and yield stress. In the numerical models incorporating DPCD material model, the elements associated with the development of "tensile" cracks possess the following characteristics:

(1) The pressure in the element is negative (tensile stress) immediately before the moment of failure (or yielding).
(2) The yield stress in the element has a rapidly decreasing trend immediately before the moment of failure (or yielding).

Table 1
Parameters used in material model.

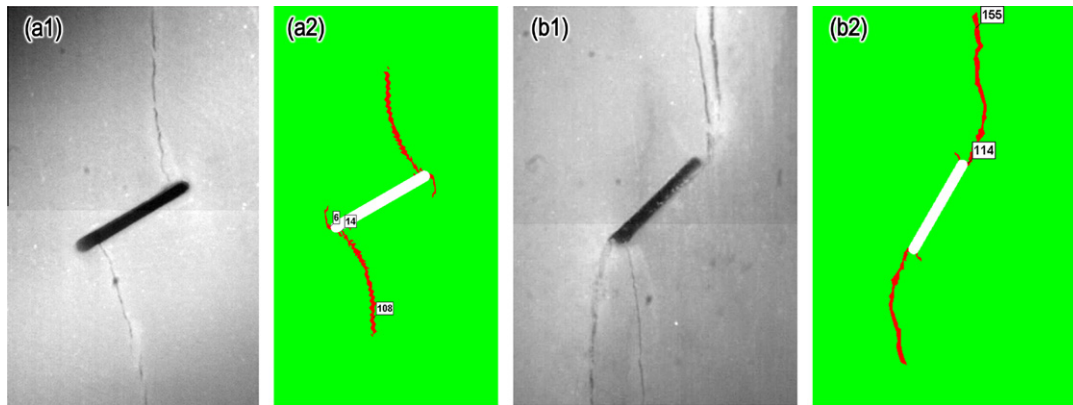|		
Density (g/cm^3)		2.44
Bulk modulus (kPa)		2.7E+07
Shear modulus (kPa)		2.2E+07
Drucker-Prager Model (kPa)	Pressure #1	−1.2e+3
	Yield stress #1	0
	Pressure #2	−1.e+3
	Yield stress #2	2.0e+4
	Pressure #3	0
	Yield stress #3	2.5e+4
	Pressure #4	8.0e+4
	Yield stress #4	1.1e+5
	Pressure #5	1.1e+5
	Yield stress #5	1.6e+5
	Pressure #6	2.0e+5
	Yield stress #6	1.95e+5
CD failure criterion	EPS1	1e−4
	EPS2	1e−3
	Maximum damage (D_{max})	0.6

Fig. 11. Two comparisons of the experimental and numerical simulation results (a) Tensile wing cracks, (b) Horsetail cracks (mixed shear–tensile cracks) (Li and Wong, 2011; Wong and Li, 2011).
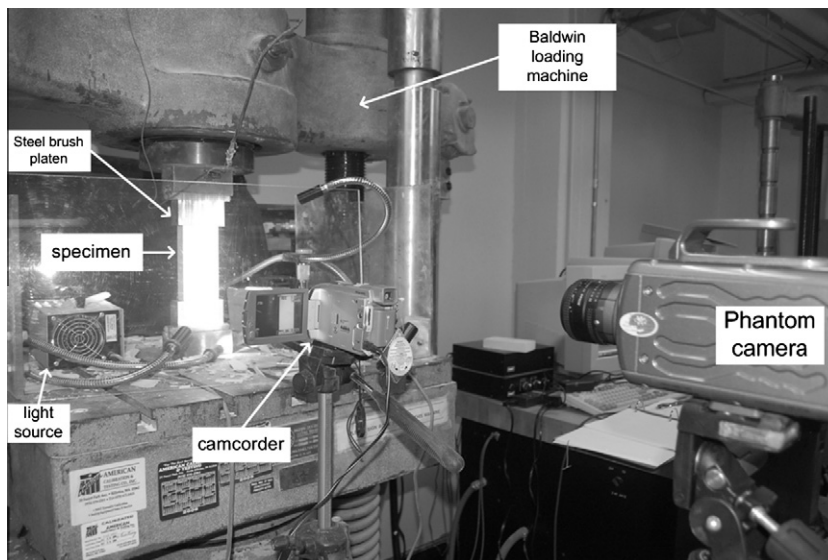

Fig. 12. Experimental setup for uniaxial compression test (Wong, 2008).

(3) The pressure, Mises stress and yield stress in the element all become zero after the tensile crack opening event.

And the element failure associated with "shear" crack initiation and propagation has the following characteristics:

(1) The pressure in the element is positive (compressive stress) immediately before the moment of yielding.
(2) The yield stress has an increasing trend immediately before the moment of yielding.
(3) The rate of increase of the Mises stress is higher than that of the yield stress immediately before the moment of yielding.
(4) The pressure, Mises stress and yield stress do not necessarily return to zero after the cracking event.

The above two distinct sets of characteristics in the elements in response to the initiation of tensile crack and shear crack were used in the present numerical study.

In our previous study (Li and Wong, submitted for publication), the influences of the element mesh pattern, namely quadrilateral structured-mesh, quadrilateral unstructured-mesh, and triangular unstructured-mesh on the crack trajectories were studied (Fig. 13). The triangular unstructured-mesh, which has the minimum influence, is adopted in the present study. Though the influence of mesh cannot be completely eliminated, the result is considered satisfactory for the purpose of our present study. Besides the meshing style, the element size also influences the precision of the simulation results. If a small element size is adopted, a smooth and refined simulated crack trajectory will be obtained. Conversely, if a too large element size is adopted, the simulated crack trajectory will be very coarse and appear undulating. Optimizing the computation time and precision of the simulation results, we choose an element size to ensure that more than ten elements are present on the flaw tip. Consequently, in our simulation results, more than 10 crack initiation positions can be differentiated around the flaw tip.

3.2. Crack initiation position

A total of six models of different flaw inclination angles were studied, with inclination angle varying from 0° to 90° at an interval of 15°. Prior to crack initiation, the ratio of Mises stress to yield stress in a particular element can reveal how close a particular element in the material to the yielding state is. A ratio equal to 1 indicates that yielding has already occurred in that particular element. In the context of the present study, material failure in the specimen would appear as a result of the further development of yielding.

For the convenience of describing the initiation position of tensile crack and shear crack at the same flaw tip region in the subsequent numerical analysis, the position along the flaw perimeter will be described with reference to the system as shown in Fig. 14, which is different from that shown in Fig. 3.

Figs. 15–20 contain the numerical results for six models, each containing a differently-inclined pre-existing flaw, subjected to the vertical loading direction. In these figures, the crack trajectories were denoted by the failed material with the maximum damage factor (D_{max} = 0.6). For each flaw inclination the crack type at the crack initiation point was labeled. The first cracks initiated in the simulated results all belonged to tensile cracks. The present numerical study revealed that when the flaw inclination angle was small (θ = 0°, 30°, 45°), tensile cracks would preferentially continue to propagate once they initiated as compared to the shear cracks. When the flaw inclination angle was large (θ = 60°, 75°, 90°), the further propagation from the early stage tensile cracks appeared to be inhibited, while the further propagation of shear cracks was favored. It should be highlighted that the shear cracks here referred to the short crack segments initiated from the flaw tips. Our previous studies (Li and Wong, 2011; Wong and Li, 2011) found that, as shear cracks further propagated, the subsequent crack segments would typically evolve to become tensile crack segments. The eventual cracks would then become the mixed shear-tensile cracks.

Below each of the above cracking image, the corresponding plot of the variation of pressure, yield stress, Mises stress and ratio of Mises stress to yield stress with the position on the flaw perimeter at the moment of shear crack initiation was included (Figs. 15–20b). A crack would initiate at the position where the Mises stress to yield stress ratio was equal to 1. Its crack type can be revealed from the associated pressure. If the corresponding pressure at the crack initiation point was positive (compressive stress), the crack would be a shear crack. If the corresponding pressure at the crack initiation point was negative (tensile stress) or zero, the crack would be a tensile crack.

Tensile crack initiation was much earlier than shear crack initiation. When a shear crack initiated, one or more tensile cracks had already initiated. The failed elements along the tensile crack trajectories could no longer bear the tensile stress. Hence the pressure at the tensile crack initiation points was zero in Figs. 15b–20b. Recall in the present study that the shear failure, or shear crack initiation, occurred after the Mises stress reached the yield stress, which did not necessarily correspond to the maximum Mises stress. However, it just happened to our model that the location of shear failure also corresponded to where maximum Mises stress was.

The crack initiation positions obtained from the AUTODYN analysis as shown in Figs. 15–20 were consistent with the generalizations derived from the FEM analysis in Section 2.3. The shear crack initiated at the point where the first principal stress (compressive stress) direction was tangent to the flaw perimeter. The
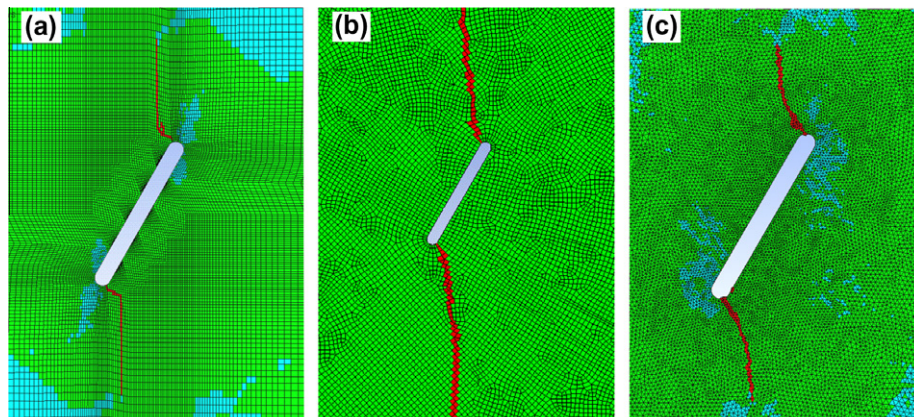

Fig. 13. Tensile wing cracks obtained in three different mesh models: (a) quadrilateral structured-mesh, (b) quadrilateral unstructured-mesh and (c) triangular unstructured-mesh.
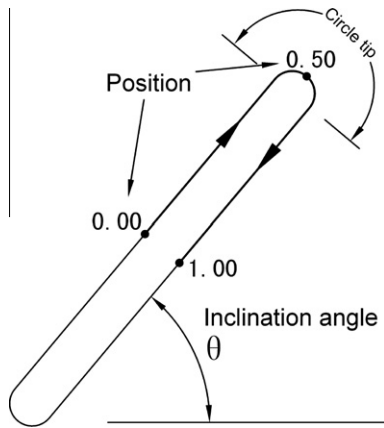
Fig. 14. Definition of position along the flaw perimeter and the flaw inclination angle in the AUTODYN numerical analysis.
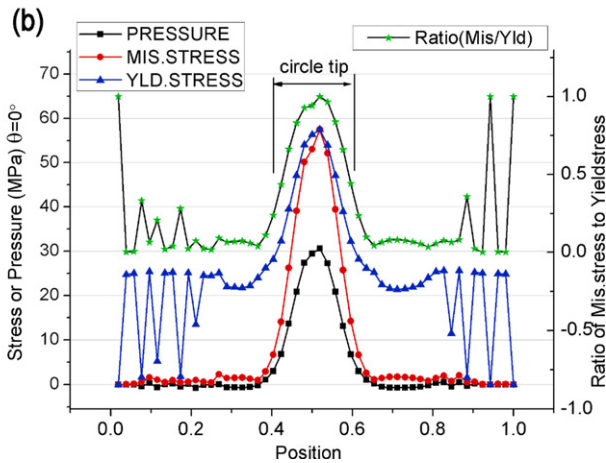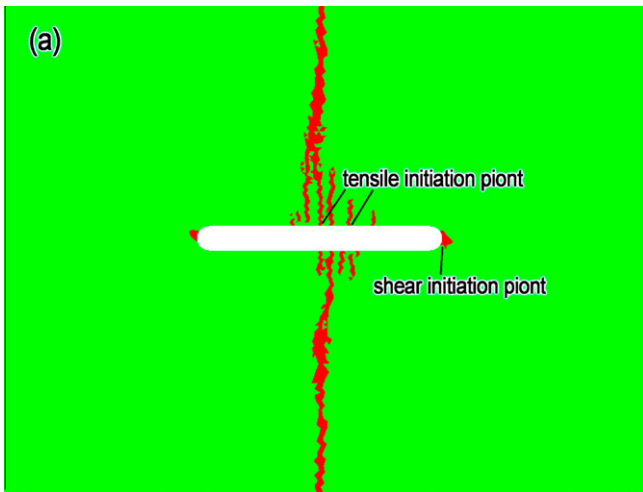

Fig. 15. Crack phenomena and stress state ($\theta = 0°$).

Fig. 16. Crack phenomena and stress state ($\theta = 30°$).

tensile crack initiation points were close to the flaw tip on the flaw perimeter, but deviating towards the flaw center. The crack initiation position would become farther away from the flaw tip for more shallowly-inclined flaws.

3.3. Influence on crack trajectory

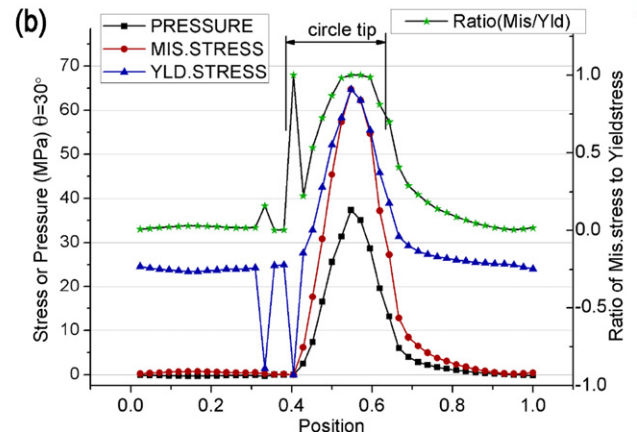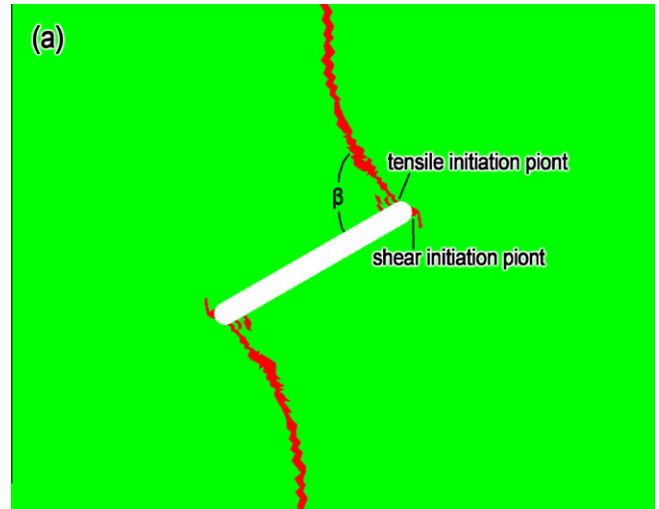The crack initiation angle, β (Fig. 16a) between the initial tensile crack segment and the pre-existing flaw was found to vary with the flaw inclination angle in the previous experimental studies (Park and Bobet, 2010; Wong, 2008). The present numerical analysis also revealed that the flaw inclination angle had a strong influence not only on the crack initiation position, but also on the shape of the crack trajectory. In the present numerical study, β was independently determined from AUTODYN analyses. β was directly measured from the crack trajectory diagrams obtained from the AUTODYN analyses as shown in Figs. 15a–20a. Fig. 21 summarizes the β values determined from AUTODYN analyses results. The laboratory data determined from the molded gypsum models were included for reference.

As shown in Fig. 21, β values obtained from the AUTODYN analysis were generally larger than the experimental data. Nonetheless, from both the numerical and physical experimental studies, β generally increased with the flaw inclination angle with a slightly decreasing trend from $\theta = 0°$ to 30°.

As a tensile wing crack initiated and propagated away from the pre-existing flaw, the crack trajectory gradually curved towards the vertical loading direction. For the tensile cracks shown in Figs. 15a–20a, the curvature of the tensile crack trajectory was more pronounced for the more shallowly-inclined flaws (small inclination angle). By identifying the location of the sharp curvature change of the propagating crack path, the initial relatively straight tensile wing crack segment was noticed to be generally longer in the shallowly-inclined flaw models than those in the steeply-inclined flaw (large inclination angle) models. For the models with an approximately vertical straight flaw, i.e. θ is near 90°, the tensile
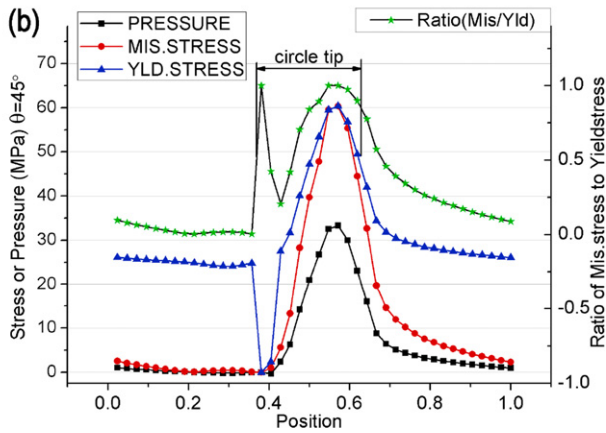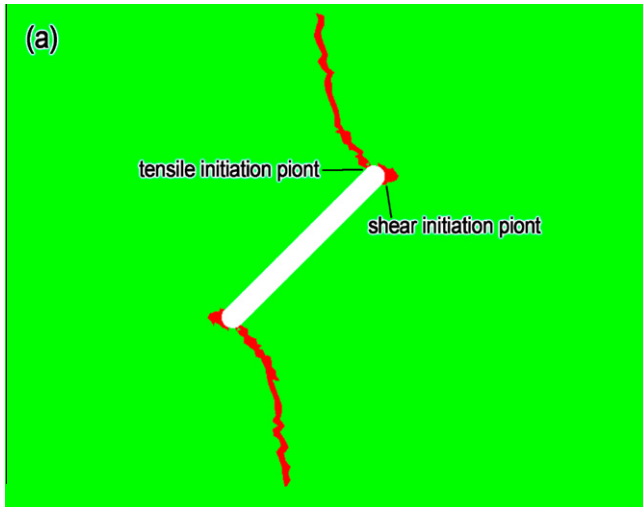
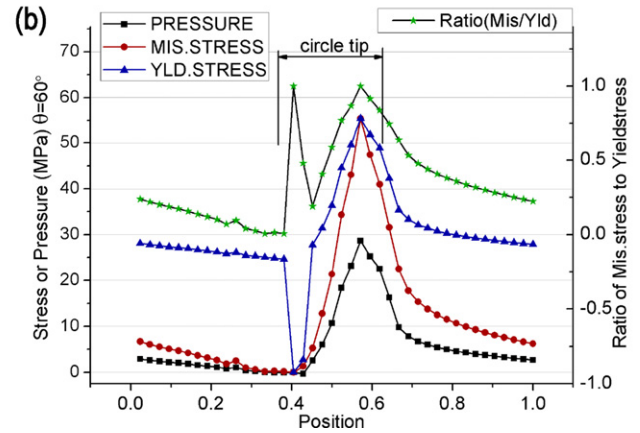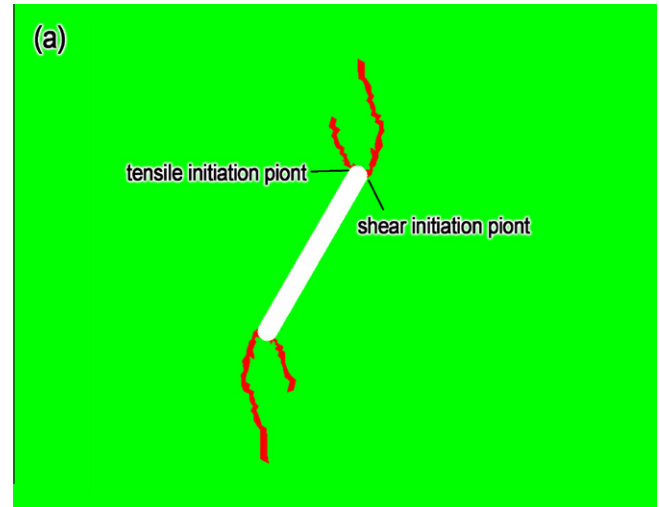**Fig. 17.** Crack phenomena and stress state ($\theta = 45°$).

Fig. 18. Crack phenomena and stress state ($\theta = 6°$).

crack trajectories were straight and their curvature was not conspicuous.

The AUTODYN numerical results also revealed the influence of flaw inclination angle on the crack propagation in response to the external loading. According to Figs. 15–20, tensile cracks always initiated prior to shear cracks, no matter how large the pre-existing flaw inclination angle was. However, for the more steeply-inclined flaws, from which tensile cracks and shear cracks had already initiated during the early stage of loading, continued loading favored further crack propagation of the shear cracks, while that of the tensile cracks was inhibited.

4. Influence of loading conditions on cracking processes

Besides the influence of pre-existing flaw inclination angle, the influence of loading conditions on the crack initiation and propagation were also analyzed in this study. In the present study, different loading conditions were obtained by varying the loading rate (R, Fig. 22) and the magnitude of maximum applied loading pressure (P_0, Fig. 22).

4.1. Influence of loading rate

In common laboratory and field loading situations, loading applied to a rock body is typically time-dependent, which can be described by the loading rate R. The loading rate refers to the magnitude of the time-dependent loading applied to the body in unit

time, as shown in Fig. 22. If the loading rate is very low and the dynamic effect is small enough to be ignored, the problem can be considered as static or quasi-static. If the loading rate is high, the load applied to the model would be time-dependent. The problem should then be considered as dynamic. Within our current context of studying pre-cracked rock specimens under a vertical loading, the models with low loading rates can be approximated as static problems and the models with high loading rates are considered to be the dynamic loading problems. In the following study, dynamic problems with different loading rates were examined.

The present dynamic analysis is concerned about the interaction of the material with the stress wave, which propagates from the pressure boundary towards the model interior. Any particular point in the numerical model is influenced by the pressure boundary only when the associated stress wave reaches the point. In other words, the point will not experience the boundary pressure until the stress wave arrives.

4.1.1. Numerical models

The present numerical investigation of the effect of loading conditions was based on the numerical models of the same dimensions (Fig. 1, $\theta = 60°$) and material parameters (Table 1) as those of the previously studied AUTODYN models. Nine different loading conditions (Table 2) were selected and applied to the models.

4.1.2. Influence of loading rate on crack phenomena

The nine different loading conditions (Table 2) ranged from low loading rate to high loading rate, which were related to different
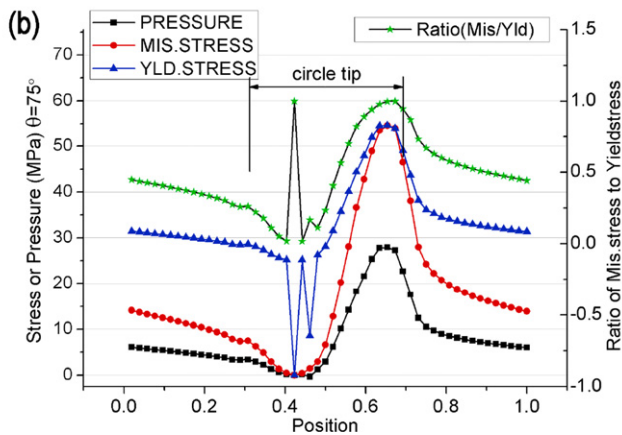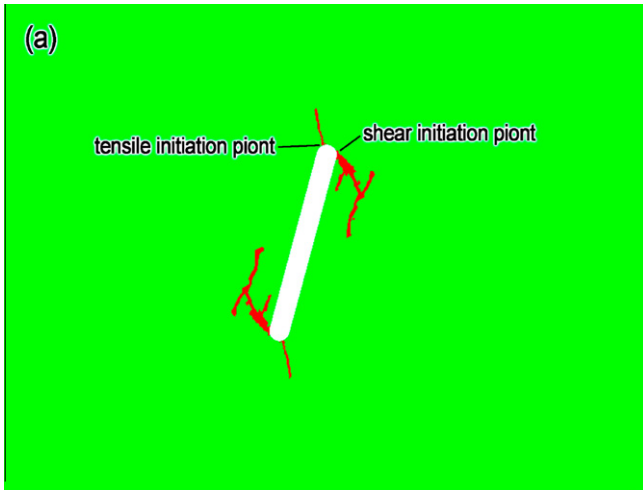
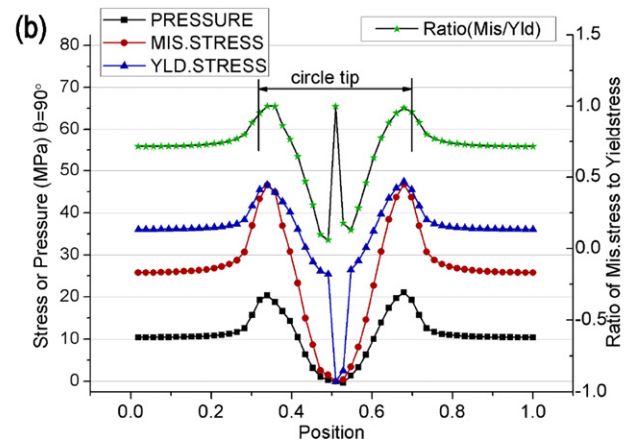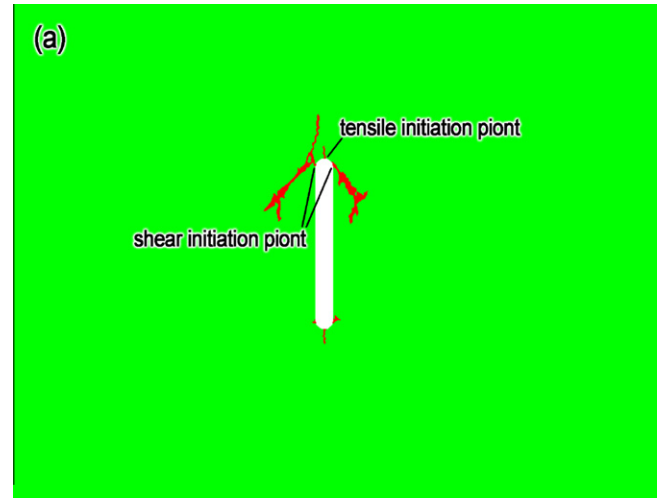**Fig. 19.** Crack phenomena and stress state ($\theta = 75°$).

Fig. 20. Crack phenomena and stress state ($\theta = 90°$).

combinations of the maximum pressure (P_0, Fig. 22) and the ramp time (T_0, Fig. 22). From the preliminary analysis involving a wide range of loading rates, when the loading rate was less than a certain threshold value, the resulting crack patterns were found to be similar. Three representative crack patterns, which were due to the low, medium and high loading rates, are shown in Figs. 23–25 respectively.

Based on the AUTODYN numerical results, the initiation of tensile crack and shear crack was each associated with distinct mechanics characteristics (mentioned in Section 3.1.3). This property was relied on in the present study to differentiate tensile cracks from shear cracks initiated from the pre-existing flaws under different loading rates. As shown in Fig. 23 to Fig. 25, "T" and "S" denoted the tensile crack and shear crack, respectively. From the numerical results, under a low loading rate (Fig. 23), the tensile cracks were observed to initiate earlier than the shear cracks. Under a medium loading rate, tensile cracks and shear cracks initiated almost simultaneously (Fig. 24). Under a high loading rate, shear cracks initiated earlier than the tensile cracks instead (Fig. 25). The crack initiation sequences established under the nine different loading conditions are listed in the last column of Table 2.

Apart from the crack initiation sequence, the loading rate also influenced the tensile crack initiation position on the flaw perimeter. Refer to the two different loading rates of Figs. 23 and 25 as an example. Under a low loading rate pressure boundary (Fig. 23), the tensile crack initiation point is at gauge No. 17 (shown in Fig. 26), but under a high loading rate pressure boundary (Fig. 25), the tensile crack initiation point is at gauge No. 15 (shown in Fig. 26).
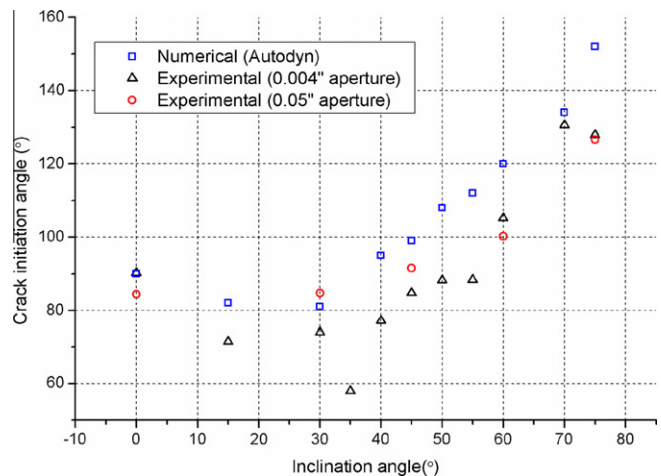
Fig. 21. Variation of the crack initiation angles between tensile crack and pre-existing flaw. The experimental data were based on laboratory tests by Wong and Einstein (2006).

4.1.3. Mechanics information about the influence of loading rate

The above numerical analysis, which focused on the phenomenal cracking behavior, showed that loading rates had an influence on the initiation sequence of tensile cracks and shear cracks. In order to account for that phenomenon, the underlying mechanism of

Fig. 22. Schematic illustration of loading condition.

Table 2
Different loading conditions and resultant crack initiation sequences.

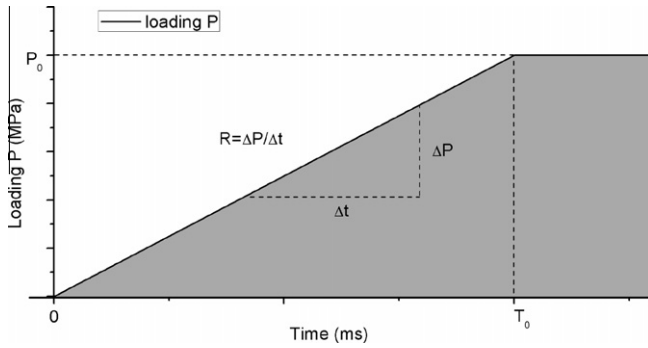| Loading condition ID	Loading rate, R (MPa/ms)	P_0 (kPa)	T_0 (ms)	Crack initiation sequence generalized from the present numerical study
1	1.25E+00	2.50E+04	20	T, S
2	2.50E+01	2.50E+04	1	T, S
3	6.25E+02	2.50E+04	0.04	T, S
4	7.14E+02	2.50E+04	0.035	T & S
5	8.33E+02	2.50E+04	0.03	S, T
6	1.25E+03	2.50E+04	0.02	S, T
7	1.25E+04	2.50E+04	0.002	S, T
8	Infinity	2.50E+04	0	S, T
9	Infinity	2.50E+03	0	T

Note: ''T'' and ''S'' denote tensile crack and shear crack respectively. ''T, S'' denotes that the initiation of tensile crack occurs prior to that of shear crack, and vice versa for ''S, T''. ''T & S'' indicates an almost simultaneous initiation of both tensile crack and shear crack.

stress wave propagation associated with different loading rates in intact numerical models and pre-cracked numerical models were investigated.

The evolution of the pressure field in an intact model of the same dimensions as that of the pre-cracked model (Fig. 1) under different loading rates was first studied (Fig. 27).

Assume the external pressure was applied to the model at time = 0 s. Fig. 28 shows the pressure distribution along the model center line starting from the top pressure boundary to the model center under two different loading rates (loading condition ID = 2 and 7) at time 0.008 ms. As shown in Fig. 28, the pressure gradient in the material induced by the higher loading rate (bottom curve) was much higher than that of lower loading rate (upper curve). In other words, the pressures at points in front of and right behind the stress wavefront were vastly different. As for a particular point, when the stress wave arrived, the pressure at the point under the higher loading rate would increase more rapidly than that under the lower loading rate over the same short time interval.

To study the mechanism of crack initiation sequence in a pre-cracked specimen, three gauges (Nos. 15, 17 and 24) were set around the pre-existing flaw tip (Fig. 26) in the two numerical models as shown earlier in Fig. 23 and Fig. 25. Gauge No. 24 was located at the shear crack initiation point. Gauge Nos. 17 and 15 were located at the tensile crack initiation point due to a low loading rate (loading condition ID = 2) and a high loading rate (loading condition ID=8), respectively. The variation of pressure, Mises stress and yield stress with time recorded at the three gauges are plotted in Fig. 29. The diagram on the left (low loading rate) provided the mechanics explanation of an earlier tensile crack initiation, while that on the right (high loading rate) provided the mechanics explanation of an earlier shear crack initiation.

The material at the tensile crack initiation point responded very differently to the two loading conditions. Under the low loading rate (Fig. 29a(ii)), the pressure at gauge No. 17 soon became negative (tensile stress) since the commencement of the externally applied loading and it remained negative until the initiation of tensile crack. In contrast, under the high loading rate (Fig. 29b(ii)), the pressure at gauge No. 15 stayed positive (compressive stress) at the beginning. The pressure later turned to negative (tensile stress), leading to the initiation of a tensile crack.

Under the high loading rate condition as shown in Fig. 29b, the pressure and stresses at gauge No. 24, which was the future shear crack initiation point, increased rapidly in the initial stage, as well as at gauges Nos. 15 and 17. Because the stress wave was compressive, the arrival of the stress wave at a particular point would lead to the immediate increase of pressure and stress at the point, even at the future tensile crack initiation points.

Fig. 30 shows the pressure variations at gauge No. 17 (Fig. 26), which was the potential tensile crack initiation point on the flaw perimeter, under different loading rates. A higher loading rate
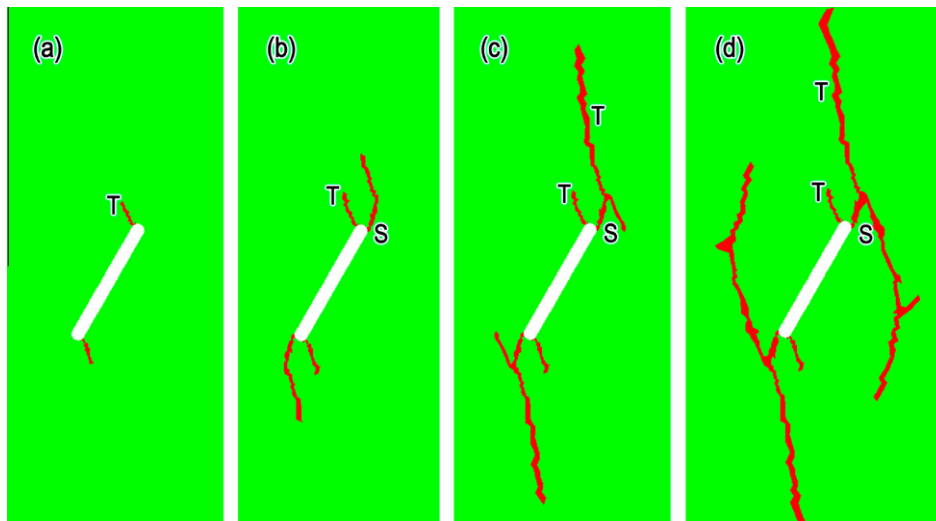

Fig. 23. Initiation and propagation of cracks under loading condition ID = 2 (low loading rate).
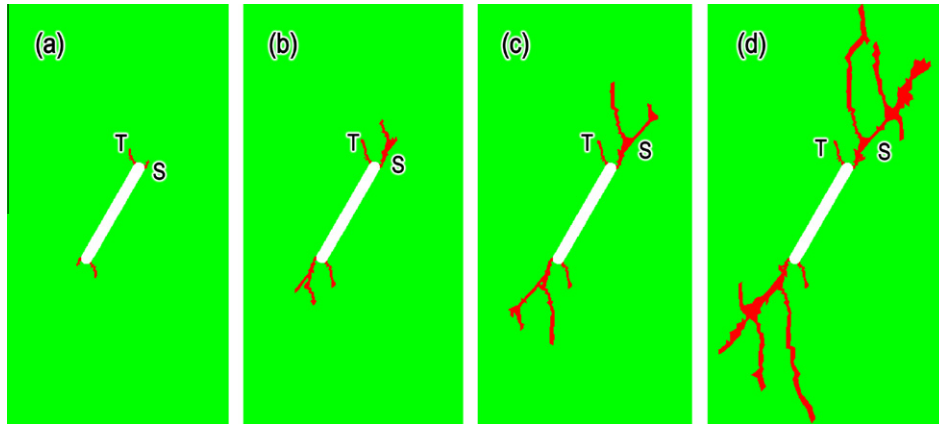
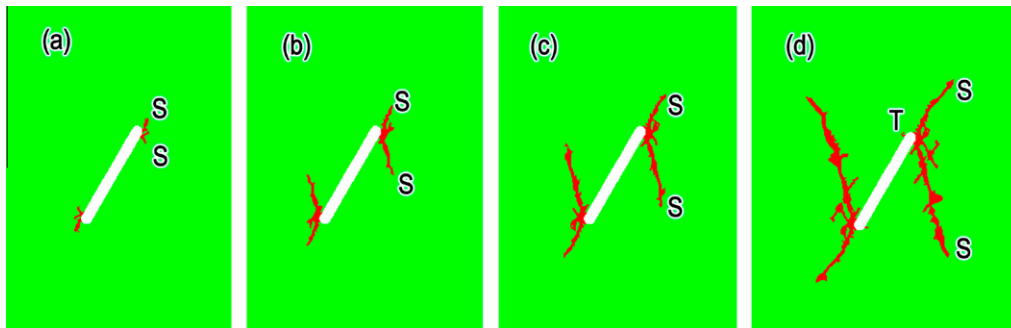**Fig. 24.** Initiation and propagation of cracks under loading condition ID = 4 (medium loading rate).

Fig. 25. Initiation and propagation of cracks under loading condition ID = 8 (high loading rate).
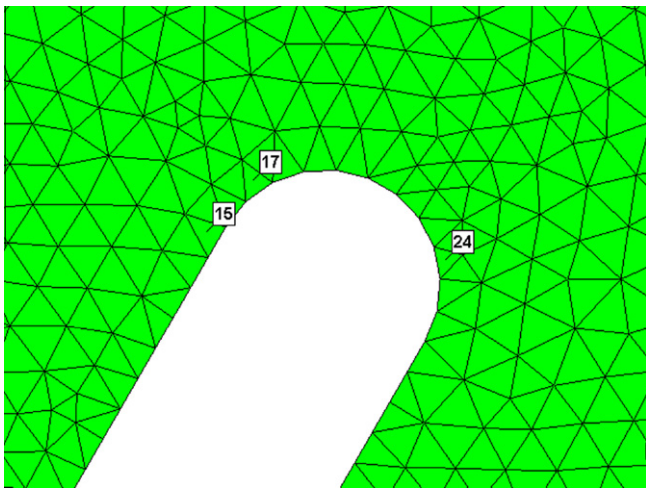

Fig. 26. Three gauges set around the pre-existing flaw tip for mechanics analysis.

Fig. 27. Schematic illustration of model.

would induce a larger compressive stress at gauge No. 17 upon the arrival of the stress wavefront. It was then followed by some oscillations in the pressure (still compressive). It later became negative before the initiation of a tensile crack. If the loading rate was low enough (such as $R \leqslant 1250$ MPa/ms), the induced compressive stress at gauge No. 17 was so small relative to the rock strength that it could be neglected. The mechanical response of the pre-existing flaw with regard to crack initiation under the high loading rate situation was thus very different from the low loading rate situation.

To sum up, at the tensile crack initiation point, a compressive stress was first induced due to the arrival of stress wave, which

later turned into a tensile stress when the stress wave passed. At the shear crack initiation point, however, stress was compressive due to the arrival of the stress wave. According to Fig. 28, the rate of increase of pressure at the point under the higher loading rate was higher than that under the lower loading rate. If the loading rate at the pressure boundary was high enough, the compressive
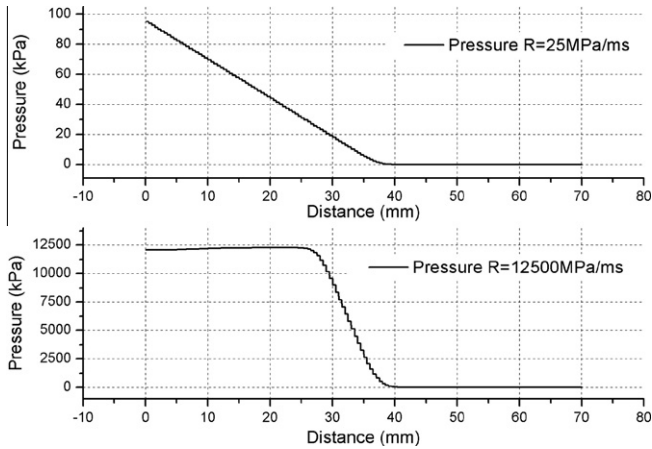
Fig. 28. Pressure variation with distance in models with loading condition ID = 2 (upper curve) and ID = 7 (bottom curve) at time = 0.008 ms since the application of the external pressure.

stress at the shear crack initiation point induced by the arrival of stress wave would be high enough to fail the material, leading to shear crack initiation. While the stress at the future tensile crack initiation point induced by the arrival of stress wave was compressive, and no tensile crack would have initiated at that moment. Therefore, under a high loading rate pressure boundary, a shear crack instead of a tensile crack would first initiate.

If the loading rate at the pressure boundary was low enough, the magnitude of the compressive stress at the future shear crack initiation point was too low to fail the material. However, at the tensile initiation point, the compressive stress induced by the arrival of stress wave would rapidly decrease and became tensile stress, hence leading to the initiation of a tensile crack. Therefore, under a low loading rate pressure boundary, tensile crack would initiate first.

4.2. Influence of maximum loading pressure

The analysis above, which showed that the loading rate had a significant influence on the crack initiation sequence, was based on the premise that the maximum boundary loading pressure was large enough with respect to the material strength. The following analyses will focus on models under the loading conditions with a high loading rate, but a much smaller maximum boundary loading pressure.

Fig. 31 shows the crack initiation and propagation processes due to the same loading rate as that of the model shown in Fig. 25, but with a ten times smaller maximum loading pressure. Due to a smaller maximum loading pressure, tensile cracks first initiated from the flaw tips, which were followed by the initiation and propagation of a pair of horizontal cracks. The initiation of shear cracks previously observed in Fig. 25c was absent in Fig. 31.

To understand the crack formation mechanism subjected to the smaller maximum loading pressure, gauges Nos. 17 and 24 were set around the pre-existing flaw tip as shown in Fig. 31c. The variations of pressure, Mises stress and yield stress recorded at the two gauges are shown in Fig. 32.

The relationship of pressure, Mises stress and yield stress at gauge No. 17 (Fig. 32a) indicated that the steeply inclined crack initiated from the flaw perimeter was a tensile crack (Fig. 31c). To account for the different crack types initiated at gauge No. 24 under different maximum loading pressures, the relationship of pressure, Mises stress and yield stress at gauge No. 24 was studied (Fig. 32b).

Because the analysis is a dynamics analysis, pressures and stresses in the model were undulating with time. As shown in Fig. 32b, the variation of the pressure, Mises stress and yield stress followed a wave form consisting of two major crests and two major troughs. Around the stress wave trough, the minimum value of pressure was negative, i.e., tensile stress. Since the tensile strength value of geomaterial is typically very low, tensile cracks are easy to initiate as the wave trough passes. Fig. 33 shows the variations of Mises
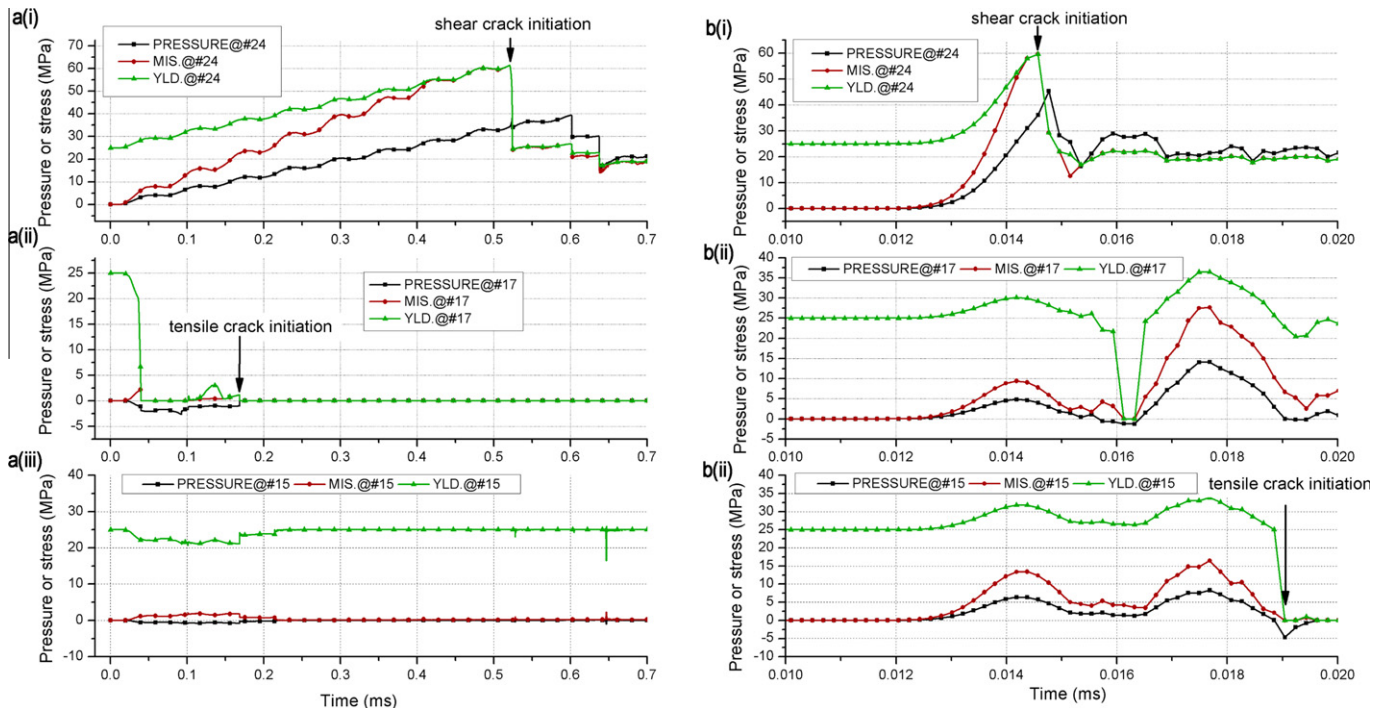

Fig. 29. Variation of pressure, Mises stress and yield stress with time due to (a) low loading rate (loading condition ID = 2) and (b) high loading rate (loading condition ID = 8).
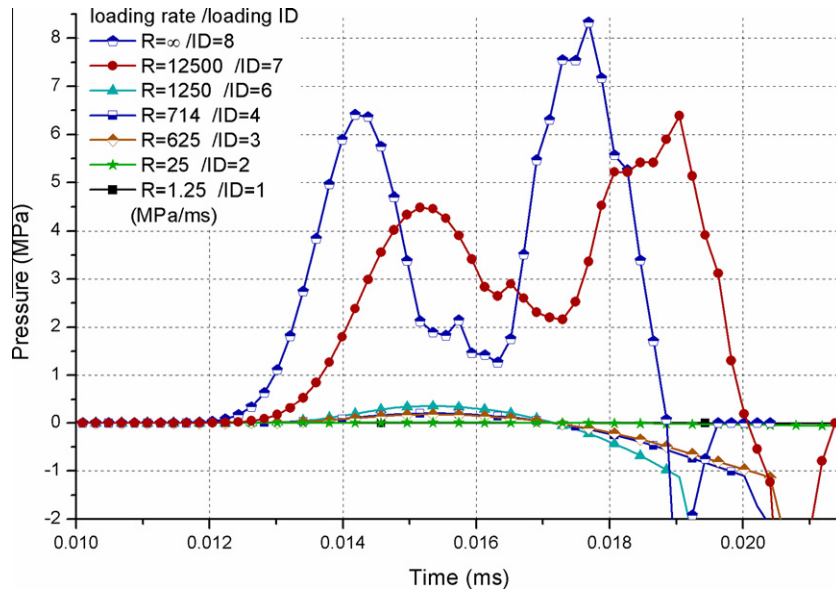
Fig. 30. Variation of pressure with time at gauge No. 17.

stress and yield stress with pressure at gauge No. 24 over two periods (C1 and C2), which are indicated in Fig. 32b. As shown in Fig. 33a, in period C1, the tensile stress caused some damage in material. The difference between P1 and P2 revealed that the strength declined before and after the occurrence of damage. As shown in Fig. 33b, in period C2, though the Mises stress reached the yield stress transiently under a compressive stress (pressure > 0), very little damage was caused. The major damage in period C2 was caused by tensile stress (pressure < 0). The point P3 in Fig. 33b indicated that the material tensile strength was zero after the major damage. Fig. 32 also showed that, after the tensile crack initiation, the pressure, Mises stress and yield stress all returned to zero, which was in accordance with our previous observations (Section 3.1.3). Therefore, gauge point No. 24 was also a tensile crack initiation point.

The above analysis suggested that the crack type and crack pattern were affected not only by the loading rate, but also the maximum loading pressure applied. In particular, when the maximum of loading pressure was small enough with respective to the material strength, even if a high loading rate was applied, the initiation of tensile crack was favored, while that of shear crack was suppressed.

5. Summary

5.1. Influence of pre-existing flaw inclination angle

(1) According to the finite element method (FEM) simulation results of a rectangle specimen containing a straight pre-existing open flaw, which was loaded vertically, the flaw inclination angle had a significant influence on the stress field around the flaw. The FEM simulation results revealed that for the flaws of a small inclination angle, tensile cracks tended to initiate close to the flaw center, at a distance away from the flaw tip. As the flaw became steeper (larger inclination angle), the tensile crack initiation position shifted towards the circular flaw tip region. In contrast, the shear crack initiation position was restricted to the circular flaw tip region.

(2) The present study attempted to generalize the initiation position of the shear crack and tensile crack. Generally, the shear crack initiation point is the point where the maximum principal stress (compressive stress) direction is tangent to the flaw edge. For the tensile crack initiation point, if the flaw is symmetrical with respect to the maximum principal
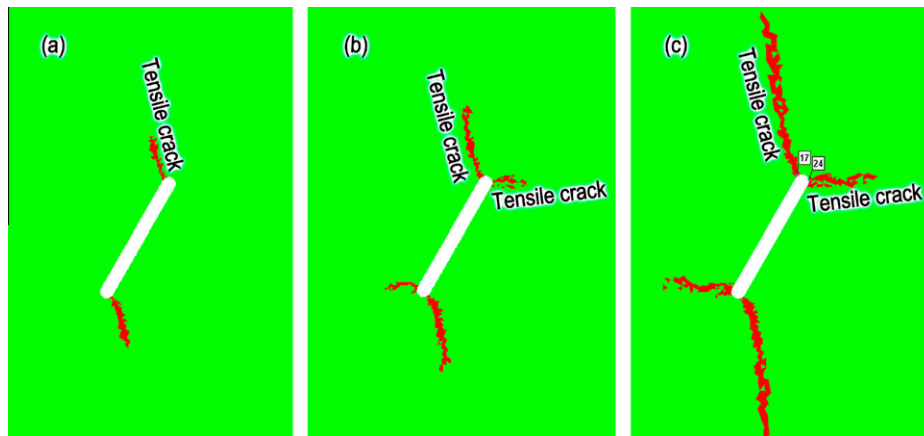

Fig. 31. Initiation and propagation of cracks under loading condition ID = 9 (high loading rate).
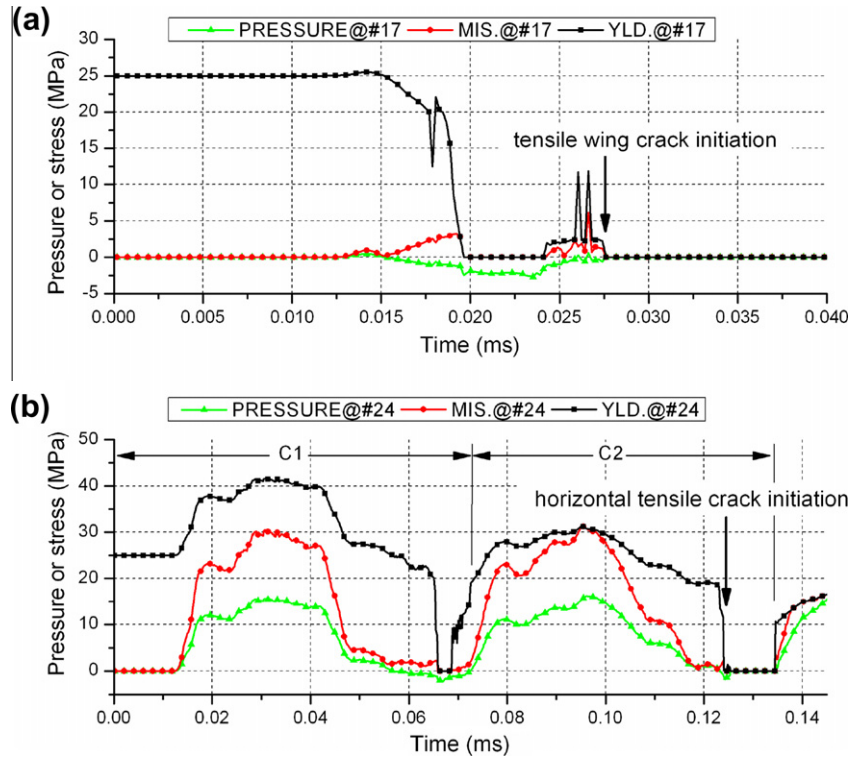
Fig. 32. Variations of pressure, Mises stress and yield stress with time at (a) gauge No. 17 and (b) gauge No. 24 (loading condition ID = 9).
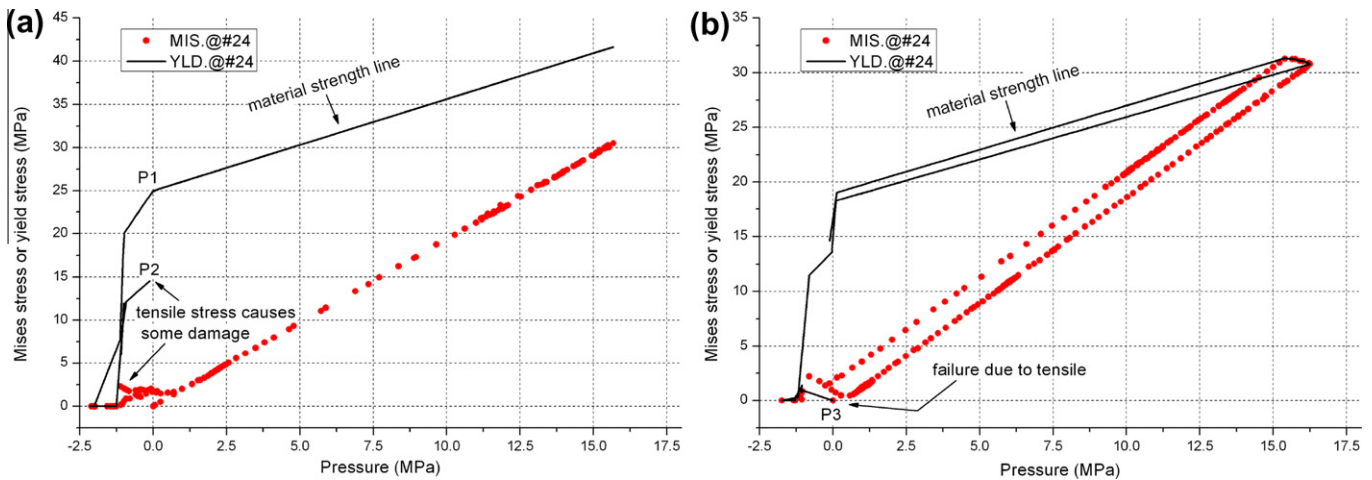

Fig. 33. Variations of Mises stress and yield stress with pressure at gauge No. 24 (a) in period C1 of Fig. 32b and (b) in period C2 of Fig. 32b.

stress direction, the tensile crack initiation position will be the intersecting points of the symmetrical axis and the flaw perimeter. For other flaw inclination angles, the tensile crack initiation position will deviate from the top point of flaw. The deviated distance varies with the flaw inclination angle and it becomes smaller for steeper flaws.

(3) According to AUTODYN simulation results, the curvatures of the tensile crack trajectory in the models containing flaws of small inclination angle were more pronounced than that in models containing flaws of large inclination angle. The initial relatively straight tensile wing crack segments were found to be generally longer in the models containing flaws of small inclination angle than those in the models containing flaws of large inclination angle.

(4) As for the crack initiation angles (β), although AUTODYN numerical results did not exactly match the experimental data in general, the significant trend of variation was captured. When flaw inclination angle was small ($\theta < 40°$), the angle β was an acute angle close to 90°. When the flaw inclination angle was larger, the angle β would increase with the increase of flaw inclination angle.

5.2. Influence of loading conditions

(1) According to the AUTODYN simulation results, loading rates had great influences on crack type and crack pattern. Under a low loading rate, the tensile cracks were observed to initiate earlier than the shear cracks. Under a medium loading

rate, tensile cracks and shear cracks initiated almost simultaneously. Under a high loading rate, shear cracks initiated earlier than the tensile cracks instead.

(2) Beside the loading rate, the maximum magnitude of the loading pressure also influenced the crack pattern. According to the numerical simulation results, the shear crack would initiate first under the loading condition with a high loading rate and a large magnitude of maximum loading pressure. The tensile crack would initiate first under the loading condition with a low loading rate or a small magnitude of maximum loading pressure. When the magnitude of maximum loading pressure was small enough, even if the loading rate was very high, the tensile cracks would initiate first and even no shear crack would initiate.

5.3. Limitations and future studies

The numerical results presented in this study were based on the Drucker–Prager strength model along with the cumulative damage failure criterion. The simulated cracking phenomena from this material model are in a good accordance with the experimental phenomena, despite that the material model is not perfect in theory to describe the tensile crack initiation. The small triangular

6. Conclusions

The primary goal of this paper is to investigate the influence of pre-existing flaw inclination angle and loading conditions on the crack initiation and propagation processes in a pre-cracked rock specimen. The numerical analysis was based on the finite element method (FEM) and non-linear dynamics method (AUTODYN). The numerical simulation results revealed that the pre-existing flaw inclination angle had a great influence on crack initiation position, propagation angles and propagation priority. With regard to the loading conditions, it could be concluded from the present study that under a relatively low loading rate or a small magnitude of maximum loading pressure, tensile cracks would tend to initiate prior to shear cracks. In contrast, under a relatively high loading rate and a large magnitude of maximum loading pressure, shear cracks would tend to initiate prior to tensile cracks instead. The study of the influence of loading condition on cracking phenomena showed that different loading conditions led to different crack patterns. The crack pattern caused by quasi-static load was very different from the crack pattern caused by blasting load or high speed impact load. This research thus contributes to those rock engineering problems in which crack initiation and propagation play an important role.

Appendix A

Stress values along the flaw perimeter determined from the FEM analysis.

Inclination angle (θ, °)	Maximum third principal stress (σ_3)		Maximum pressure (P)				Maximum Mises stress (σ_v)	
	Position	σ_3/σ_0	Position	Tensile pressure (P/σ_0)	Position	Compressive pressure (P/σ_0)	Position	σ_v/σ_0
0	0.535	−0.996	0.535	−0.432	0.004	3.470	0.004	6.960
5	0.748	−1.040	0.748	−0.452	0.004	3.430	0.011	6.810
10	0.908	−1.160	0.908	−0.509	0.004	3.380	0.004	6.660
15	0.926	−1.480	0.926	−0.652	0.018	3.390	0.018	6.800
20	0.926	−1.780	0.933	−0.804	0.018	3.370	0.018	6.710
25	0.933	−2.090	0.933	−0.949	0.025	3.350	0.025	6.650
30	0.933	−2.400	0.933	−1.060	0.025	3.280	0.018	6.520
35	0.940	−2.550	0.940	−1.120	0.032	3.210	0.025	6.480
40	0.940	−2.670	0.940	−1.180	0.039	3.150	0.039	6.370
45	0.940	−2.640	0.940	−1.160	0.039	3.040	0.032	6.080
50	0.940	−2.490	0.940	−1.080	0.046	2.920	0.039	5.640
55	0.954	−2.322	0.947	−1.017	0.046	2.741	0.039	5.494
60	0.961	−2.079	0.954	−0.914	0.053	2.621	0.053	5.178
65	0.961	−1.847	0.961	−0.806	0.053	2.359	0.046	4.749
70	0.968	−1.602	0.968	−0.704	0.053	2.099	0.060	4.204
75	0.975	−1.313	0.975	−0.525	0.053	1.660	0.053	3.797
80	0.982	−1.172	0.982	−0.514	0.060	1.556	0.060	3.057
85	0.989	−1.039	0.989	−0.454	0.060	1.255	0.060	2.539
90	0.004	−0.894	0.004	−0.380	0.067	0.864	0.067	1.963

unstructured-mesh and cumulative damage failure criterion were adopted in this numerical study to minimize the influence of mesh. Although the influence of the mesh cannot be completely eliminated, the simulated results were considered good enough and competent for the study. To our best knowledge, related experimental work investigating the influence of loading rates on detailed crack development processes in rocks under dynamic loading was limited. The present study thus provides the basis for the future pursuit of experimental study, which can in turn help verify the numerical results associated with dynamic loading problems on rock.

References

Atkinson, B.K., 1987. Fracture Mechanics of Rock, first ed. Elsevier, London.

Backers, T., Fardin, N., Dresen, G., Stephansson, O., 2003. Effect of loading rate on Mode I fracture toughness, roughness and micromechanics of sandstone. Int. J. Rock Mech. Min. 40, 425–433.

Bazant, Z.P., Gettu, R., 1992. Rate effects and load relaxation in static fracture of concrete. ACI Mater. J. 89, 457–468.

Bieniawski, Z.T., 1967. Mechanism of brittle fracture of rock: Part II–experimental studies. Int. J. Rock Mech. Min. 4, 407–408 (IN413-IN414, 409–418, IN415-IN418, 419–423).

Biolzi, L., Tognon, G., 1987. Strain rate effect on crack propagation in concrete. Theor. Appl. Fract. Mech. 7, 201–206.

Brace, W.F., Bombolakis, E.G., 1963. A note on brittle crack growth in compression. J. Geophys. Res. 68, 3709–3713.

Chen, G., Kemeny, J., Harpalani, S., S, 1993. Fracture propagation and coalescence in marble plates with pre-cut notches under compression. Int. J. Rock Mech. Min. 30, 279.

Chen, C.S., Pan, E., Amadei, B., 1998. Fracture mechanics analysis of cracked discs of anisotropic rock using the boundary element method. Int. J. Rock Mech. Min. 35, 195–218.

Chiarelli, M., Frediani, A., Lucchesi, M., 1996. Computation of crack extension energy rate for elastic–plastic hardening materials under variable loading. Eng. Fract. Mech. 55, 813–830.

Einstein, H.H., Dershowitz, W.S., 1990. Tensile and shear fracturing in predominantly compressive stress fields – a review. Eng. Geol. 29, 149–172.

Erdogan, G., Sih, G.-C., 1963. On the crack extension in plates under plane loading and transverse shear. ASME J. Basic Eng. 85, 519–527.

Griffith, A.A., 1920. The phenomena of rupture and flow in solids. Philos. Trans. Roy. Soc. Lond. 221, 163–198.

Hancock, P.L., 1985. Brittle microtectonics: principles and practice. J. Struct. Geol. 7, 437–457.

Hoelzer, D.T., Ali, J.A., Ebrahimi, F., 1986. A study of the correlation between crack tip opening displacement (CTOD) and stretch zone width (SZW). Scripta Metall. Mater. 20, 1575–1580.

Huang, J.F., Chen, G.L., Zhao, Y.H., Ren, W., 1990. An experimental study of the strain field development prior to failure of a marble plate under compression. Tectonophysics 175, 269–284.

Ingraffea, A.R., Heuze, F.E., 1980. Finite element models for rock fracture mechanics. Int. J. Numer. Anal. Met. 4, 25–43.

Irwin, G.R., Liebowitz, H., Paris, P.C., 1968. A mystery of fracture mechanics. Eng. Fract. Mech. 1, 235–236.

Karihaloo, B.L., 1979. Note on complexities of compression failure. Proc. Roy. Soc. Lond. A: Mater. 368, 483–493.

Kendall, K., 1978. Complexities of compression failure. Proc. Roy. Soc. Lond. A: Mater. 361, 245–263.

Koppenhoefer, K.C.D., Robert, H., Jr., 1997. A numerical investigation of loading rate effects on pre-cracked charpy V-notch specimens. Civil Engineering Studies SRS-618. University of Illinois Engineering Experiment Station, pp. 1–175.

Lajtai, E.Z., 1974. Brittle fracture in compression. Int. J. Fract. 10, 525–536.

Lajtai, E.Z., Carter, B.J., Ayari, M.L., 1990. Criteria for brittle fracture in compression. Eng. Fract. Mech. 37, 59–74.

Lauterbach, B., Gross, D., 1998. Crack growth in brittle solids under compression. Mech. Mater. 29, 81–92.

Li, H.Q., Wong, L.N.Y., 2011. Initiation and propagation of tensile wing cracks and horsetail cracks from a pre-existing flaw under compression (ARMA 11-341). In: 45th US Rock Mechanics/Geomechanics Symposium, San Francisco, CA, United states.

Li, H.Q., Wong, L.N.Y., submitted for publication. Cracking processes in specimens containing single flaws under uniaxial compression – a numerical study. Int. J. Fracture.

Li, Y.P., Chen, L.Z., Wang, Y.H., 2005. Experimental research on pre-cracked marble under compression. Int. J. Solids Struct. 42, 2505–2516.

Maiti, S.K., Smith, R.A., 1984. Criteria for brittle fracture in biaxial tension. Eng. Fract. Mech. 19, 793–804.

Maligno, A.R., Rajaratnam, S., Leen, S.B., Williams, E.J., 2010. A three-dimensional (3D) numerical study of fatigue crack growth using remeshing techniques. Eng. Fract. Mech. 77, 94–111.

McMillan, J.C., Pelloux, R.M., 1970. Fatigue crack propagation under programmed loads and crack tip opening displacements. Eng. Fract. Mech. 2, 81–82, in87-in88, 83-84.

Nemat-Nasser, S., 1985. Mechanics of brittle failure in compression. Comput. Struct. 20, 235–237.

Ouinas, D., Bouiadjra, B.B., Serier, B., Benderdouche, N., Ouinas, A., 2009. Numerical analysis of Brazilian bioceramic discs under diametrical compression loading. Comput. Mater. Sci. 45, 443–448.

Ožbolt, J., Rah, K., Meštrović, D., 2006. Influence of loading rate on concrete cone failure. Int. J. Fracture 139, 239–252.

Palmer, I.G., Brindley, B.J., Harrison, R.P., 1974. The relationship between acoustic emission and crack opening displacement measurements. Mater. Sci. Eng. 14, 3–6.

Park, C.H., Bobet, A., 2010. Crack initiation, propagation and coalescence from frictional flaws in uniaxial compression. Eng. Fract. Mech. 77, 2727–2748.

Pearce, C.J., Thavalingam, A., Liao, Z., Bicanic, N., 2000. Computational aspects of the discontinuous deformation analysis framework for modelling concrete fracture. Eng. Fract. Mech. 65, 283–298.

Persson, A., 1991. CM1 – a simple model for the dynamic deformation and failure properties of brittle materials. In: 4th International Symposium on Ceramic Materials and Components for Engines. Dynamec Research AB, Gothenburg, Sweden.

Petit, J.P., Barquins, M., 1988. Can natural faults propagate under mode II conditions. Tectonics 7, 1243–1256.

Potyondy, D.O., Cundall, P.A., 2004. A bonded-particle model for rock. Int. J. Rock Mech. Min. 41, 1329–1364.

Radjy, F., Hansen, T.C., 1973. Fracture of hardened cement paste and concrete. Cement Concrete Res. 3, 343–361.

Rannou, J., Limodin, N., Réthoré, J., Gravouil, A., Ludwig, W., Baïetto-Dubourg, M.-C., Buffière, J.-Y., Combescure, A., Hild, F., Roux, S., 2010. Three dimensional experimental and numerical multiscale analysis of a fatigue crack. Comput. Methods Appl. M 199, 1307–1325.

Reinhardt, H.W., Weerheijm, J., 1991. Tensile fracture of concrete at high loading rates taking account of inertia and crack velocity effects. Int. J. Fracture 51, 31–42.

Rispoli, R., 1981. Stress fields about strike-slip faults inferred for stylolites and tension gashes. Tectonophysics 75, 29–36.

Rossmanith, H.P., 1983. Rock fracture mechanics. Springer.

Schreyer, H.L., 2007. Modelling surface orientation and stress at failure of concrete and geological materials. Int. J. Numer. Anal. Met. 31, 147–171.

Sommer, E., Soltész, U., 1971. Crack-opening-displacement measurements of a dynamically loaded crack. Eng. Fract. Mech. 2, 235–238.

Sreeramulu, K., Sharma, P., Narasimhan, R., Mishra, R.K., 2010. Numerical simulations of crack tip fields in polycrystalline plastic solids. Eng. Fract. Mech. 77, 1253–1274.

Sullivan, A.M., Crooker, T.W., 1977. A crack-opening-displacement technique for crack length measurement in fatigue crack growth rate testing – development and evaluation. Eng. Fract. Mech. 9, 159–166.

Tang, C.A., 1997. Numerical simulation of progressive rock failure and associated seismicity. Int. J. Rock Mech. Min. 34, 249–261.

Tang, C.A., Kou, S.Q., 1998. Crack propagation and coalescence in brittle materials under compression. Eng. Fract. Mech. 61, 311–324.

Tang, C.A., Liu, H., Lee, P.K.K., Tsui, Y., Tham, L.G., 2000. Numerical studies of the influence of microstructure on rock failure in uniaxial compression – Part I: Effect of heterogeneity. Int. J. Rock Mech. Min. 37, 555–569.

Tham, C.Y., 2005. Reinforced concrete perforation and penetration simulation using AUTODYN-3D. Finite Elem. Anal. Des. 41, 1401–1410.

Vanel, L., Ciliberto, S., Cortet, P.P., Santucci, S., 2009. Time-dependent rupture and slow crack growth: elastic and viscoplastic dynamics. J. Phys. D: Appl. Phys. 42, 214007–214019.

Wang, E.Z., Shrive, N.G., 1993. On the griffith criteria for brittle fracture in compression. Eng. Fract. Mech. 46, 15–26.

Wang, E.Z., Shrive, N.G., 1995. Brittle fracture in compression: mechanisms, models and criteria. Eng. Fract. Mech. 52, 1107–1126.

Wawersik, W.R., Fairhurst, C., 1970. A study of brittle rock fracture in laboratory compression experiments. Int. J. Rock Mech. Min. 7, 561–575.

Webb, T.W., Aifantis, E.C., 1970. Loading rate dependence of stick-slip fracture in polymers. Mech. Res. Commun. 24, 115–121.

Weber, W., Willner, K., Kuhn, G., 2010. Numerical analysis of the influence of crack surface roughness on the crack path. Eng. Fract. Mech. 77, 1708–1720.

Wells, A.A., 1969. Crack opening displacements from elastic–plastic analyses of externally notched tension bars. Eng. Fract. Mech. 1, 399–410.

Willemse, E.J.M., Peacock, D.C.P., Aydin, A., 1997. Nucleation and growth of strike-slip faults in limestones from Somerset. UK J. Struct. Geol. 19, 1461–1477.

Wong, N.Y., 2008. Crack coalescence in molded gypsum and carrara marble. Massachusetts Institute of Technology.

Wong, L.N.Y., Einstein, H., 2006. Fracturing behavior of prismatic specimens containing single flaws. In: 41st US Rock Mechanics Symposium. Omnipress, Golden, CO, United States.

Wong, L.N.Y., Einstein, H.H., 2009a. Crack coalescence in molded gypsum and carrara marble: Part 1. Macroscopic observations and interpretation. Rock Mech. Rock. Eng. 42, 475–511.

Wong, L.N.Y., Einstein, H.H., 2009b. Crack coalescence in molded gypsum and carrara marble: Part 2 – Microscopic observations and interpretation. Rock Mech Rock Eng 42, 513–545.

Wong, L.N.Y., Einstein, H.H., 2009c. Systematic evaluation of cracking behavior in specimens containing single flaws under uniaxial compression. Int. J. Rock Mech. Min. 46, 239–249.

Wong, L.N.Y., Li, H.Q., 2011. Initiation and propagation of tensile wing cracks and anti-wing cracks from a pre-existing open flaw under compression (ISRM11-0283). In: Zhou, Q. (Ed.), 12th ISRM International Congress on Rock Mechanics. TAYLOR & FRANCIS GROUP, London, UK, Beijing, China.

Wong, R.H.C., Guo, Y.S.H., Li, L.Y., Chau, K.T., Zhu, W.S., Li, S.C., 2006. Anti-wing crack growth from surface flaw in real rock under uniaxial compression. In: 16th European Conference on Fracture (EFC16), Alexandroupolis, Greece. p. 825.

Xia, K., Nasseri, M.H.B., Mohanty, B., Lu, F., Chen, R., Luo, S.N., 2008. Effects of microstructures on dynamic compression of Barre granite. Int. J. Rock. Mech. Min. 45, 879–887.

Yamamoto, I., Mukaiyama, T., Yamashita, K., ZhengMing, S., 2004. Effect of loading rate on absorbed energy and fracture surface deformation in a 6061-T651 aluminum alloy. Eng. Fract. Mech. 71, 1255–1271.

Yoon, J.H., Lee, B.S., Oh, Y.J., Hong, J.H., 1999. Effects of loading rate and temperature on J-R fracture resistance of an SA516-Gr. 70 steel for nuclear piping. Int. J. Pres. Ves. PIP 76, 663–670.

Zhang, X.X., Ruiz, G., Yu, R.C., Tarifa, M., 2009. Fracture behaviour of high-strength concrete at a wide range of loading rates. Int. J. Impact. Eng. 36, 1204–1209.

Zhang, H.H., Li, L.X., An, X.M., Ma, G.W., 2010. Numerical analysis of 2-D crack propagation problems using the numerical manifold method. Eng. Anal. Bound Elem. 34, 41–50.

Zhao, L.G., Tong, J., Hardy, M.C., 2010. Prediction of crack growth in a nickel-based superalloy under fatigue-oxidation conditions. Eng. Fract. Mech. 77, 925–938.

Zhou, X.-p., Qian, Q.-h., Yang, H.-q., 2010. Effect of loading rate on fracture characteristics of rock. J. Cent. South Univ. T. 17, 150–155.

Zielinski, A.J., 1984. Model for tensile fracture of concrete at high rates of loading. Cement Concrete Res. 14, 215–224.